



### Experimental and Numerical Study of Auxetic Sandwich Panels on 160 grams of PE4 Blast Loading

Journal:	<i>Journal of Sandwich Structures and Materials</i>
Manuscript ID	JSSM-20-0132.R1
Manuscript Type:	Standard Article
Date Submitted by the Author:	18-Jun-2020
Complete List of Authors:	Arifurrahman, Faizal; Cranfield University, Survivability Lethality and Advanced Materials Group, Centre for Defence Engineering; Institut Teknologi Bandung, Lightweight Structures Research Group, Faculty of Mechanical and Aerospace Engineering Critchley, Richard; Cranfield University, Survivability Lethality and Advanced Materials Group, Centre for Defence Engineering Horsfall, Ian; Cranfield University, Survivability Lethality and Advanced Materials Group, Centre for Defence Engineering
Keywords:	Blast loading, experimental study, sandwich panel, air gap, foam, auxetic, deflection
Abstract:	Mines, specifically as Anti-Tank (AT) mines are a significant threat for defence vehicles. While approaches such as v-shaped hulls are currently used to deflect the blast products from such threats, such a solution is not always usable when hull standoff is limited. As such the development of a low profile, energy absorbing solution is desirable. One approach that has potential to achieve these requirements are sandwich panels. While sandwich panel cores can be constructed from various materials, one material of particular interest are auxetics. Auxetic are materials that exhibit a negative Poisson's ratio. This material has potential to be an efficient an impact energy absorber by increasing stiffness at local deformation by gathering mass at the impact location. This study investigates the effectiveness of novel auxetic core infills alongside three other panel types (monolithic, air gap, polymer foam sandwich) against buried charges. 160 grams of PE4 were buried in 100 mm depth and 500 mm stand off the target. Laser and High Speed Video (HSV) system were used to capture the deflection-time profile and load cell sensors were used to record the loading profile received by the panels. Experimental

1  
2  
3  
4  
5  
6  
7  
8  
9  
10  
11  
12  
13  
14  
15  
16  
17  
18  
19  
20  
21  
22  
23  
24  
25  
26  
27  
28  
29  
30  
31  
32  
33  
34  
35  
36  
37  
38  
39  
40  
41  
42  
43  
44  
45  
46  
47  
48  
49  
50  
51  
52  
53  
54  
55  
56  
57  
58  
59  
60

	<p>works were compared with numerical model. Explicit model were generated in LSDYNA software as 'initial impulse mine' keyword. The result found that the auxetic and foam core panels were effective in reducing peak structural loading and impulse by up to 33% and 34% respectively. Air-filled panels were the most effective to reduce the deflection of the rear of the plate, however variation between capture methods (HSV and Laser system) were reported, while numerical modelling provided comparable plate deflections responses. When normalised against panel weight, the air filled panels were experimentally the most efficient per unit mass system with the auxetics being the least effective.</p>

SCHOLARONE™  
Manuscripts

# 1                    2                    3                    4                    5                    6                    7                    8                    9                    10                    11                    12                    13                    14                    15                    16                    17                    18                    19                    20                    21                    22                    23                    24                    25                    26                    27                    28                    29                    30                    31                    32                    33                    34                    35                    36                    37                    38                    39                    40                    41                    42                    43                    44                    45                    46                    47                    48                    49                    50                    51                    52                    53                    54                    55                    56                    57                    58                    59                    60

## 1                    2                    3                    4                    5                    6                    7                    8                    9                    10                    11                    12                    13                    14                    15                    16                    17                    18                    19                    20                    21                    22                    23                    24                    25                    26                    27                    28                    29                    30                    31                    32                    33                    34                    35                    36                    37                    38                    39                    40                    41                    42                    43                    44                    45                    46                    47                    48                    49                    50                    51                    52                    53                    54                    55                    56                    57                    58                    59                    60

1                    2                    3                    4                    5                    6                    7                    8                    9                    10                    11                    12                    13                    14                    15                    16                    17                    18                    19                    20                    21                    22                    23                    24                    25                    26                    27                    28                    29                    30                    31                    32                    33                    34                    35                    36                    37                    38                    39                    40                    41                    42                    43                    44                    45                    46                    47                    48                    49                    50                    51                    52                    53                    54                    55                    56                    57                    58                    59                    60

1                    2                    3                    4                    5                    6                    7                    8                    9                    10                    11                    12                    13                    14                    15                    16                    17                    18                    19                    20                    21                    22                    23                    24                    25                    26                    27                    28                    29                    30                    31                    32                    33                    34                    35                    36                    37                    38                    39                    40                    41                    42                    43                    44                    45                    46                    47                    48                    49                    50                    51                    52                    53                    54                    55                    56                    57                    58                    59                    60

1                    2                    3                    4                    5                    6                    7                    8                    9                    10                    11                    12                    13                    14                    15                    16                    17                    18                    19                    20                    21                    22                    23                    24                    25                    26                    27                    28                    29                    30                    31                    32                    33                    34                    35                    36                    37                    38                    39                    40                    41                    42                    43                    44                    45                    46                    47                    48                    49                    50                    51                    52                    53                    54                    55                    56                    57                    58                    59                    60

1                    2                    3                    4                    5                    6                    7                    8                    9                    10                    11                    12                    13                    14                    15                    16                    17                    18                    19                    20                    21                    22                    23                    24                    25                    26                    27                    28                    29                    30                    31                    32                    33                    34                    35                    36                    37                    38                    39                    40                    41                    42                    43                    44                    45                    46                    47                    48                    49                    50                    51                    52                    53                    54                    55                    56                    57                    58                    59                    60

1                    2                    3                    4                    5                    6                    7                    8                    9                    10                    11                    12                    13                    14                    15                    16                    17                    18                    19                    20                    21                    22                    23                    24                    25                    26                    27                    28                    29                    30                    31                    32                    33                    34                    35                    36                    37                    38                    39                    40                    41                    42                    43                    44                    45                    46                    47                    48                    49                    50                    51                    52                    53                    54                    55                    56                    57                    58                    59                    60

## 1                    2                    3                    4                    5                    6                    7                    8                    9                    10                    11                    12                    13                    14                    15                    16                    17                    18                    19                    20                    21                    22                    23                    24                    25                    26                    27                    28                    29                    30                    31                    32                    33                    34                    35                    36                    37                    38                    39                    40                    41                    42                    43                    44                    45                    46                    47                    48                    49                    50                    51                    52                    53                    54                    55                    56                    57                    58                    59                    60

1                    2                    3                    4                    5                    6                    7                    8                    9                    10                    11                    12                    13                    14                    15                    16                    17                    18                    19                    20                    21                    22                    23                    24                    25                    26                    27                    28                    29                    30                    31                    32                    33                    34                    35                    36                    37                    38                    39                    40                    41                    42                    43                    44                    45                    46                    47                    48                    49                    50                    51                    52                    53                    54                    55                    56                    57                    58                    59                    60

1                    2                    3                    4                    5                    6                    7                    8                    9                    10                    11                    12                    13                    14                    15                    16                    17                    18                    19                    20                    21                    22                    23                    24                    25                    26                    27                    28                    29                    30                    31                    32                    33                    34                    35                    36                    37                    38                    39                    40                    41                    42                    43                    44                    45                    46                    47                    48                    49                    50                    51                    52                    53                    54                    55                    56                    57                    58                    59                    60

1                    2                    3                    4                    5                    6                    7                    8                    9                    10                    11                    12                    13                    14                    15                    16                    17                    18                    19                    20                    21                    22                    23                    24                    25                    26                    27                    28                    29                    30                    31                    32                    33                    34                    35                    36                    37                    38                    39                    40                    41                    42                    43                    44                    45                    46                    47                    48                    49                    50                    51                    52                    53                    54                    55                    56                    57                    58                    59                    60

## 1                    2                    3                    4                    5                    6                    7                    8                    9                    10                    11                    12                    13                    14                    15                    16                    17                    18                    19                    20                    21                    22                    23                    24                    25                    26                    27                    28                    29                    30                    31                    32                    33                    34                    35                    36                    37                    38                    39                    40                    41                    42                    43                    44                    45                    46                    47                    48                    49                    50                    51                    52                    53                    54                    55                    56                    57                    58                    59                    60

1  
2  
3 40 Anti-vehicle (AV) mines and Improvised Explosive Devices (IEDs) have become a feature of modern  
4 41 warfare. Since World War II, they have become the leading cause of vehicle loss <sup>1</sup>. AT mines with  
5 42 typically 6 kg of explosives can cause severe damage to the vehicle and injury or kill its occupants. Bird  
6 43 reported that 22% of the United States (U.S) military losses were due to landmines in World War II <sup>2</sup>.  
7 44 Furthermore, the percentage of fatality in the Korean War, Vietnam War, Persian Gulf operation, and  
8 45 Somalia were 55%, 70%, 59%, and 60%, respectively. NATO (North Atlantic Treaty Organisation)  
9 46 presented the data of the AV mine data in its technical report <sup>3</sup>. The data shows the number of incidents  
10 47 resulting in casualties and fatalities between the years 1998 to 2006. The quantity of accidents and  
11 48 casualties depended on the year and the conflict. The number of incidents increased during such  
12 49 disputes, such as the former Yugoslavia, Afghanistan, and Iraq conflict. During this period, there were  
13 50 approximately 255 casualties and 235 fatalities on more than 190 AV mine incidents all over the world.  
14 51 In a recent conflict, U.S overseas contingency operation of Iraq and Afghanistan, AT mines and IEDs were  
15 52 responsible for nearly half of total 4,153 US troops deaths since 2006 <sup>4</sup>.

16  
17  
18  
19  
20 53 As IEDs and AT mines continue to improve, so must the protection. The mitigation methods have  
21 54 changed with vehicle generation by designing the improved anti-land mine structures <sup>5</sup>. Whilst rolled  
22 55 homogeneous armour is traditionally used as vehicle armour, it is unsuitable in mass terms to merely  
23 56 increase thickness to protect against larger or more sophisticated mine threats. As such, various  
24 57 alternative approaches have been investigated, including structural alterations, sacrificial plates, the use  
25 58 of energy absorbing materials and alternative materials <sup>5-7</sup>.

26  
27  
28 59 However, one material yet to gain traction for vehicle mine protection are auxetics. Auxetics are a  
29 60 modern class of materials that have demonstrated Improved mechanical properties such as fracture  
30 61 toughness <sup>8-10</sup>, resilience <sup>11</sup>, shear resistance <sup>12-16</sup>, or even vibration response <sup>17-19</sup> owing to their  
31 62 negative Poisson's ratio <sup>20</sup>. The negative Poisson's ratio causes the material thicker when stretched or  
32 63 will shrink towards the centre of compression loading. The shrinkage area becomes denser to increase  
33 64 indentation resistance <sup>21-23</sup>. To date a wide range of materials have been modified to be auxetic  
34 65 including polymers <sup>24</sup>, metals <sup>12,25</sup>, ceramics <sup>26-28</sup>, composites <sup>29,30</sup>, and fibres <sup>31,32</sup>. In nature, these  
35 66 materials can be found in black phosphorus <sup>33</sup> or biological tissues <sup>34</sup>. Since their inception, several  
36 67 applications for the defence field have been proposed. In the defence field, auxetics has an opportunity  
37 68 as a shield or barrier by absorbing the impact energy <sup>35-37</sup>. The density enhancement of auxetic makes it  
38 69 possible to take in the explosion shock energy and reduce the barrier damage. The progressive crushing  
39 70 of auxetic core results in densification and concentration of material in the centre. The densification  
40 71 absorbs the impact load and reduce the back-face deflection <sup>38</sup>. More recently the concept of using  
41 72 auxetic materials as an energy absorber in blast impact mitigation have been explored <sup>39,40</sup>.

42  
43  
44  
45 73 The idea of using a core sandwich material as a blast protector is not new. Several numerical and  
46 74 analytical studies of sandwich structure responses subjected to impulse loading have been conducted <sup>40-</sup>  
47 75 <sup>46</sup>. The studies have varied materials, panel thickness, or panel configuration. In the earlier work, Schenk  
48 76 et al.<sup>42</sup> explored the stacked folded material core for sandwich configuration. Numerical modelling on  
49 77 quasi-static and dynamic loading has been executed to find the optimum core architecture for maximum  
50 78 for blast mitigation. Imbalzano conducted the numerical analysis of auxetic composite under blast  
51 79 loading <sup>41</sup>. The curvature or chiral form also been investigated to understand how the modified auxetic  
52 80 geometry effects their mechanical properties <sup>37</sup>. The experimental investigation of the blast impact on  
53 81 the monolithic panel structures have been done <sup>47-49</sup>. However, only a few studies have been  
54 82 undertaken using explosive loading due to the potential factors including cost, and accessibility.

1  
2  
3 83 Moreover, the buried explosive loading is also a rare study until present. Specifically for auxetic  
4 84 materials, Qi et al.<sup>39</sup> compared the numerical and experimental results of sandwich panels under 250  
5 85 grams of composition B explosive. They examined the areal specific energy absorption (ASEA), and the  
6 86 study indicated the potential of auxetic in the protection of civil and vehicle objects. Moreover, several  
7 87 numerical methods were compared to experimental explosive loading<sup>50</sup>. For the cellular sandwich  
8 88 panel, Holloman et al.<sup>51</sup> investigated the impulse transfer of sand impact, one key observation is that the  
9 89 strong core cellular structures transferred the same impulse as a solid block while the softer core  
10 90 transferred less impulse.

11  
12  
13 91 Furthermore, the mine explosion phenomenon shows that the short duration of explosion in  
14 92 comparison to the natural period of the vehicle structure makes the pressure-time loading is not  
15 93 relevant<sup>52,53</sup>. Otherwise, the total impulse of blast impact is a critical indicator of blast effect on the  
16 94 vehicle structure. This indicator can be approximated from the Tremblay equation<sup>54</sup>. Deflection is one of  
17 95 the parameters to measure the damage on the structure and how far mine explosion able to deflect the  
18 96 vehicle structure. Therefore, the objectives of this study are: (i) to conduct the explosion testing of 160  
19 97 grams of PE-4 explosives, which is relatively larger amount of size than the existed works, buried under  
20 98 the fine building sand (ii) to replicate the observed testing in numerical modelling; (iii) to compare the  
21 99 results between the experimental and numerical simulation; and (iv) to investigate the displacement  
22 100 and impulse response on four different panel configurations, i.e. monolithic, air gap, Styrofoam core and  
23 101 steel-made auxetic sandwich. In addition, the specific energy absorption will be presented to figure out  
24 102 the effectiveness of auxetic structures in absorbing impulse damage.

25  
26  
27  
28  
29 103

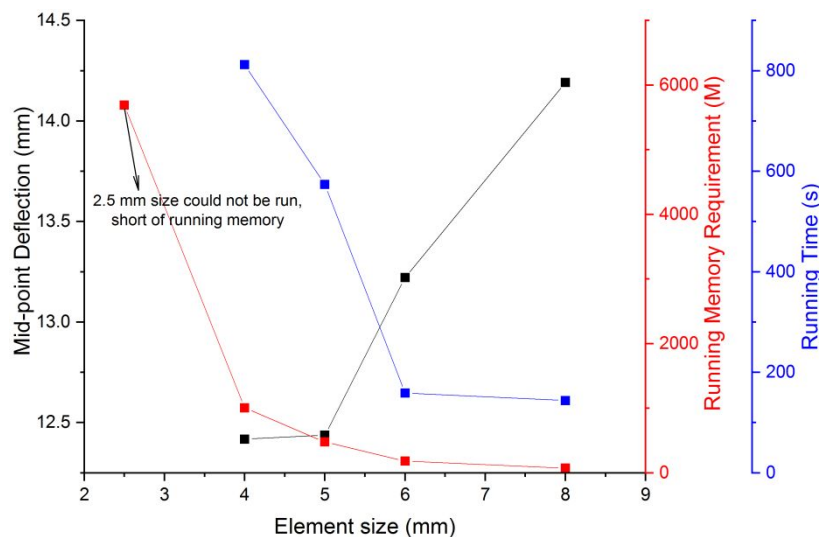
## 30 104 **2. Finite Element Modelling**

31  
32 105 Computational modelling was undertaken using LS-DYNA pre post V4.5 with the explicit solver of R910  
33 106 double-precision, using a 64 bit Windows 7, 32 GB RAM, i7 2.6 GHz 8 core processor computer. This is an  
34 107 an explicit non-linear dynamic finite element code which is appropriate for handling the dynamics  
35 108 testing and complex contact interaction between the structure sheets. The steel panels were fully  
36 109 modelled using a Belytschko-Lin-Tsay four-node thin shell element type, due to the simple and reliable  
37 110 shell element<sup>55</sup>. Element size was determined through the mesh convergence test detailed below.

### 38 111 *2.1. Mesh convergence test*

39  
40  
41  
42 112 Mesh convergence is required to obtain the optimum element size by considering numerical accuracy  
43 113 and simulation solve time. Several number of 'impulse mine' simulations were carried out to determine  
44 114 the appropriate shell element size. Shell element size of 8 mm, 6 mm, 5 mm, 4 mm, and 2.5 mm of  
45 115 auxetic sandwich panels were modelled to investigate the central node displacement and the effects of  
46 116 resolution on the simulation output, as shown in the Figure 1. It indicated that the shell element size  
47 117 affects the modelling result. The use of 8 mm and 6 mm that have a bigger element size than 5 mm and  
48 118 4 mm produced a higher deflection. 5 and 4 mm element size model is shown to be converged to the  
49 119 value of 12.4 mm. We also considered the running memory allocation to choose the proper element  
50 120 size. Memory allocation is required to process the modelling. Higher number of elements would demand  
51 121 higher memory requirement. Figure 1 indicated that reducing 1 mm size would increase the memory  
52 122 requirement by factor of 2. The running time of these simulations were not the issue because as  
53 123 presented in Figure 1 that the maximum CPU time for 4 mm running element size was only 812 s. The

124 running time was increasing when the element size was reduced. By reducing the element size by 1 mm,  
 125 the running time of auxetic panel was increasing to 1.1 to 3.6 times and the required memory to finish  
 126 the job was increasing more than double. Moreover, especially for sandwich structure that requires  
 127 complex interaction between the layer and numerous elements, thin metal shell element or foam solid  
 128 element smaller than 5 mm will result in higher computational times. Due to the relatively smaller  
 129 difference in deflection for smaller elements, the authors deemed the extra computational time  
 130 unnecessary.



131  
 132 **Figure 1:** Mesh convergence test detailing relationship between element size, maximum deflection and memory  
 133 requirement

## 134 2.2. Buried charge modelling

135 We considered that 'Initial impulse mine' were suitable in this case due to the accuracy and considered  
 136 less time consuming than other methods<sup>56</sup>. The buried charge was simulated using 'initial impulse mine'  
 137 keyword<sup>57</sup>, and was defined in terms of TNT equivalence; 160 gram mass of PE4 explosive is equivalent  
 138 to 208 gram of TNT. This rule follows Bogosian et al. study<sup>58</sup>. The 'initial impulse mine' function was  
 139 derived based on Tremblay equation<sup>54</sup>. Figure 2 shows the 'initial impulse mine' keyword conditions  
 140 which replicates the Tremblay model. Tremblay modified the empirical equation of specific impulse  
 141 (impulse per unit area) presented by Westine et al<sup>59</sup>. By integrating the specific impulse, the total  
 142 impulse was acquired. The equation below determines the total impulse for a quadrangular deflector  
 143 panel above the land mine

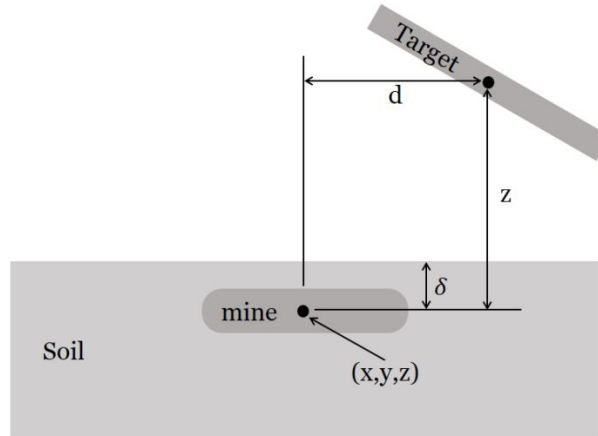
$$144 \quad i_v = k_0(S_1 + S_2) \left( 1 + \frac{7\delta}{9z} \right) \sqrt{\frac{\rho E}{z}}$$

145 Equation 1

146 where  $k_0$  is a constant,  $S_1$  and  $S_2$  are variables of the error function. These variables determine the  
 147 approximation accuracy to calculate the total impulse. Tremblay also set the non-dimensional  
 148 parameters of Westine et al. model concerning the charge position range as presented in Table 1, where  
 149  $\delta$  is depth of burial charge in [m],  $E$  is energy released by explosive charge in [J],  $A$  is cross-sectional area

1  
2  
3 150 of mine in  $[m^3]$ ,  $\rho$  is soil density in  $[kg/m^3]$ ,  $c$  is the seismic P-wave velocity in the soil in  $[m/s]$ , and  $z$  is  
4 151 standoff distance of the point of charge to the centre of mine in  $[m]$ .

6 152 Another limitation is a factor 1.8 to the empirical specific impulse. The predicted impulse occurred is  
7 153 between the interval of  $i_v/1.8$  to  $1.8i_v$ . This expected impulse is also in agreement with William et al.  
8 154 study that determined 66% correction factor to produce a good correlation with experimental  
9 155 observations<sup>60</sup>.



25 156  
26 157 **Figure 2:** 'Initial Impulse Mine' model where the explosive charge was modelled as point of charge relative to the  
27 158 depth of burial, standoff distance, and soil density<sup>54</sup>.

29 159  
30 160 **Table 1:** Tremblay's non-dimensional parameters<sup>54</sup>

	model parameter	
$0.106 \leq$	$\frac{\delta}{z} = 0.2$	$\leq 1.0$
$6.35 \leq$	$\frac{E/A}{\rho c^2 z} = 5.12$	$\leq 150$
$0.154 \leq$	$\frac{\sqrt{A}}{z} = 0.102$	$\leq 4.48$
$0 \leq$	$\frac{d}{z} = 0.4$	$\leq 19.3$

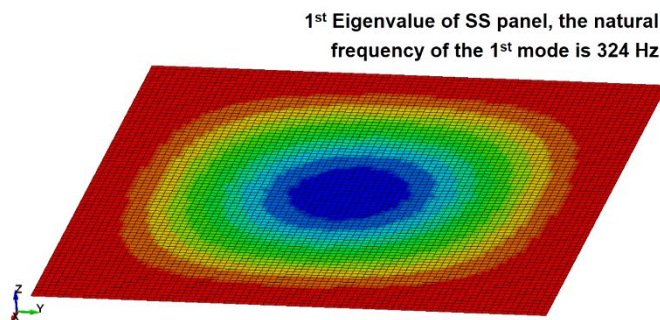
45 161  
46 162 **2.3. Boundary conditions**

48 163 The boundary condition at the panel edges were set to be fixed and simulated the clamped joint at the  
49 164 edge of the testing panel. Fix joint restrained the panel to move in six degrees of freedoms, three  
50 165 degrees of translational and three degrees of rotational.

52 166 Contact in the sandwich panels was required for air gap, foam, and auxetic core. 'Automatic surface to  
53 167 surface' contact was applied to those configurations. It defined the contact between the elements of  
54 168 panel and core as a friction contact. This contact type provided the same model according to the real

169 condition where the metal sheet only touched in the core without any adhesion or bonding. Also,  
 170 'automatic single surface' was also defined to the panel surfaces to prevent the interpenetration  
 171 between each contacting elements during the deformation.

172 Damping response also must be considered to obtain the precise structure response. The result of  
 173 energy dissipation forms damping during structural vibration, which is affected by structural damping  
 174 (material itself) and Colomb damping on the dry surface of the clamped joint. The conservation  
 175 approach neglects this interaction between the charge source in a shock wave and the structure <sup>61</sup>. In  
 176 this study, dissipated energy due to the plastic deformation is far greater than the damping energy.  
 177 However, other studies show that the damping ratio can overestimate the deflections for lighter  
 178 structure in low-level blast loads <sup>62</sup>. The effect of the damping ratio has a considered effect on the  
 179 displacement response <sup>19,63-65</sup>. We have roughly calculated to predict the damping ratio from the  
 180 overshoot of displacement trace of monolithic panels. The results indicated that the damping ratio  
 181 ranged between 5-11%. So in this study, the damping ratio coefficient in numerical will be assumed as  
 182 5% of critical damping. Figure 3 displays the first mode or critical mode of the monolithic panel occurs at  
 183 324 Hz.



185 **Figure 3:** Single steel panel simulated by modal analysis to calculate natural frequency and appropriate dampening  
 186 ratio.

#### 187 2.4. Material model

188 The steel material was modelled as an elasto-plastic material with kinematic hardening. The steel panel  
 189 was modelled using a plastic kinematic material model that ignored the effect of thermal changes due to  
 190 the limitation of material data <sup>55</sup>. This model is also used by Jin to model his plate <sup>43</sup>. A plastic kinematic  
 191 model is acceptable since the lack of stress-strain data. This material model also includes the damage  
 192 criterion when the failure stress reached. The numerical model included strain rate effects in the model  
 193 as Cowper Symonds constants of mild steel <sup>66,67</sup>. These constants are applied to the surface panels and  
 194 auxetics core. Next, the foam material was created as a crushable foam with isotropic properties <sup>68,69</sup>.  
 195 For crushable foam, strain-stress data was generated by inputting the plasticity points. The foam  
 196 element is deleted when the strain reaches the failure criterion of elongation at break. The mechanical  
 197 properties of the utilized mild steel and Styrofoam material were taken from the ASTM material  
 198 database <sup>70</sup> and technical data from Wickes Ltd. <sup>71</sup>, as shown in

199 Table 2.



200

201

**Table 2:** Steel and foam material properties

BS1449 CR4 steel properties		Styrofoam by Craftfoam blue	
Density (kg/m <sup>3</sup> )	7830.0	Density (kg/m <sup>3</sup> )	33.0
Elastic Modulus (GPa)	200	Elastic Modulus (kPa)	24
Poisson's ratio	0.29	Poisson's ratio	0.20
Yield strength (MPa)	280	Compressive strength (kPa)	50
Failure strain (%)	28		
Cowper Symonds parameter, D (s <sup>-1</sup> )	40		
Cowper Symonds parameter, q	5		

202

### 3. Experimental Work

#### 3.1. Buried charges

Twelve tests were conducted across four different panel configurations at a fixed standoff distance of 400 mm from the sand surface. A spherical charge of 160 gram PE-4 was buried at a depth of 100 mm, from the centre to the ground surface in the sand, supplied by Wickes, UK (Figure 4). The sand was naturally dried within a laboratory environment for a minimum of seven days and raked twice daily to facilitate uniform drying. Prior to the testing, the sand humidity was recorded using a WT Meter at five different locations, four on the surface, and one at the base, where the charge was placed. A summary of the humidity readings and taken test days are given in Appendix A.



212

**Figure 4:** Contained sand with centre location excavated to enable placement of PE4

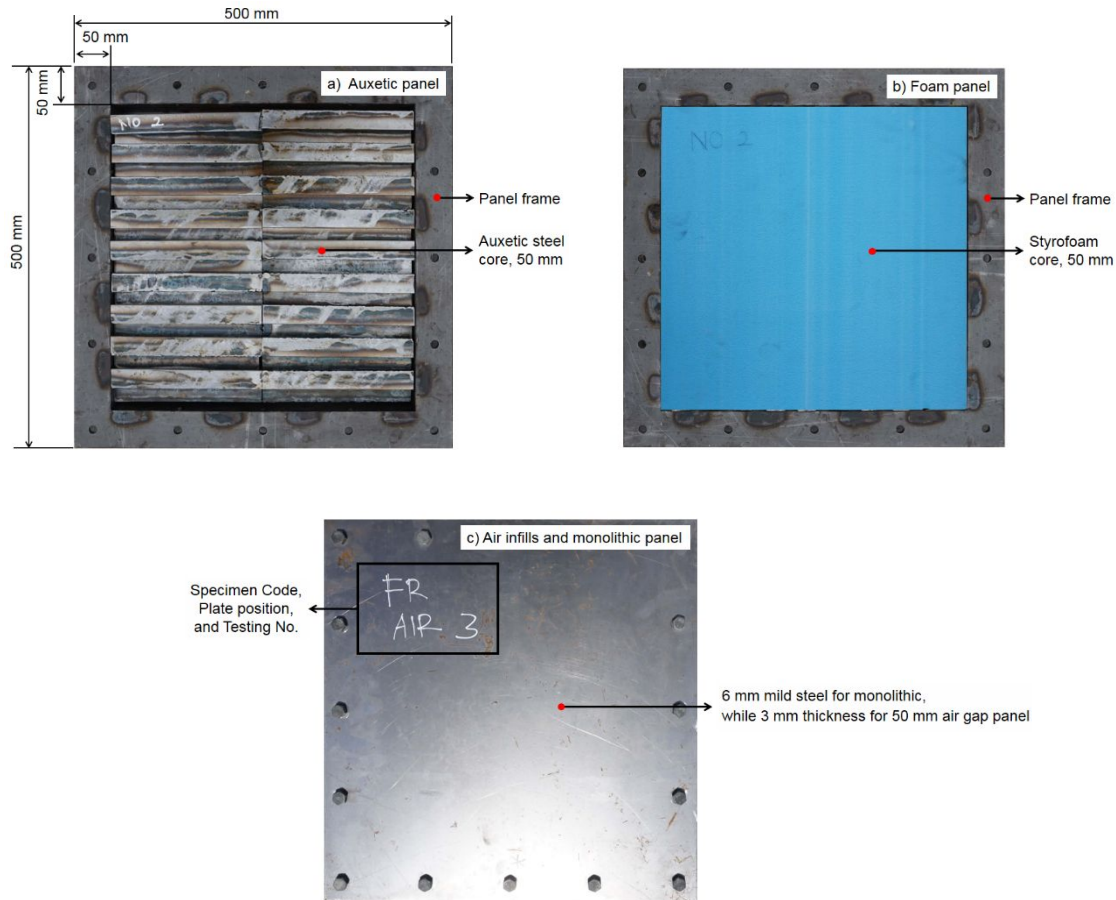
#### 3.2. Material and panel specifications

215 A series of test panels, dimensions 500 mm x 500 mm were manufactured at Cranfield University  
 216 workshops, as described in Table 3. The flat steel plates were 6mm in thickness, while the sandwich  
 217 panels comprised of four components; 2 x 3 mm steel plates, a support frame, and a core. The support  
 218 frame was manufactured from C-Bar and had external dimensions 500 mm x 500 mm x 50 mm, with  
 219 interior dimensions of 400 mm x 400 mm, as illustrated in Figure 5. A series of M10 bolt fasteners were  
 220 placed at regular intervals of distance 112.5 mm, to facilitate the fixing of the plates to the support  
 221 frame and the experimental test rig.

222 **Table 3:** Testing panel configurations used within this study

Test Number	Testing Code	Configuration	Layer Thickness (mm), in sequence
1	SS1	Single steel plate	6
2	SS2	Single steel plate	6
3	SS3	Single steel plate	6
4	SA1	Steel - Air gap - Steel	3 - 50 - 3
5	SA2	Steel - Air gap - Steel	3 - 50 - 3
6	SA3	Steel - Air gap - Steel	3 - 50 - 3
7	SF1	Steel - Styrofoam - Steel	3 - 50 - 3
8	SF2	Steel - Styrofoam - Steel	3 - 50 - 3
9	SF3	Steel - Styrofoam - Steel	3 - 50 - 3
10	SX1	Steel - Auxetic core - Steel	3 - 50 - 3
11	SX2	Steel - Auxetic core - Steel	3 - 50 - 3
12	SX3	Steel - Auxetic core - Steel	3 - 50 - 3

223

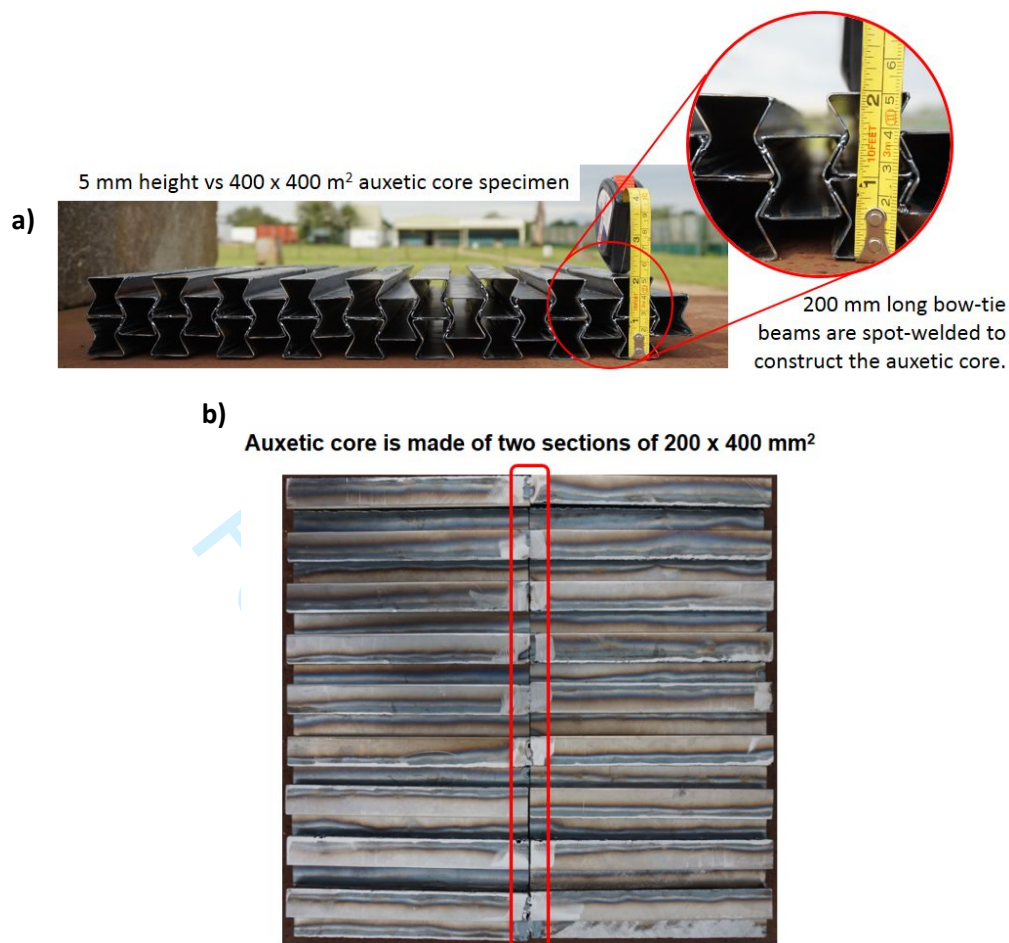


224

225

226 **Figure 5:** Panel geometry has dimension of 500 mm x 500 mm mild steel panel with the frame width of 50 mm at  
 227 each edge constraint the sample. The effective area of exploded panel is 400 mm x 400 mm. a) Auxetic sandwich  
 228 panel; b) Foam infills panel; c) Air infills and monolithic panel.

229 Three different core materials were investigated: Atmospheric air (air gap), Craftfoam Blue, and an  
 230 auxetic re-entrant structure. Craftfoam Blue, supplied by PanelSystems<sup>72</sup>, is a low-density Polystyrene  
 231 Foam typically used for model making and prototyping. Metal sheets were supplied of dimensions 600  
 232 mm x 600 mm x 50 mm, and cut down to 400 mm x 400 mm x 50 mm using a band saw. The auxetic core  
 233 was manufactured using a bending method from 1 mm sheet mild steel to a re-entrant bowtie structure  
 234 (**Figure 6**). Due to the limitation of bending tools, the 400 mm x 400 mm auxetic core was manufactured  
 235 as two 200 mm x 400 mm parts and welded to form a single core. Welding was used to join the closed  
 236 side and each bow tie pieces to create the configuration.



34 **Figure 6:** An example of the re-entrant auxetic core in a) side on and b) a top down view.

### 36 240 3.3. Data acquisitions

38 241 Experiments were undertaken on the Explosive Range and Demonstration Area (ERDA) located at the  
 39 242 Shrivenham campus of Cranfield University, over a three-day period. A custom-built support rig fixed the  
 40 243 panels, which provide rigid sample support that contain the explosives under the sample (**Figure 7**). The  
 41 244 support rig consists of three main components i.e., explosive plates, I-Beam cross sections, and frames.  
 42 245 The plates were attached to the blast rig by anchoring the corners to the underbelly of the I-beams and  
 43 246 sandwiched between two thick pieces of square steel at the top. Located between the plates and test rig  
 44 247 at opposite corners were two Piezo-electric Kistler sensors (9061A 0-200 kN). Load cells took the loading  
 45 248 data by changing the deformation of compressed cells during the explosion to the voltage signal. The  
 46 249 acquisition data convert the voltage response in the load cells to the Newton unit. Data was captured at  
 47 250 a sampling rate of 100 kHz using a Prosig 8012 acquisition system coupled with a charge amplifier. A pre-  
 48 251 trigger (triggered above 30 kN) set at 0.1 s was used to ensure event capture. A calibrated hammer  
 49 252 equipped with a load cell was used to validate the load cells.

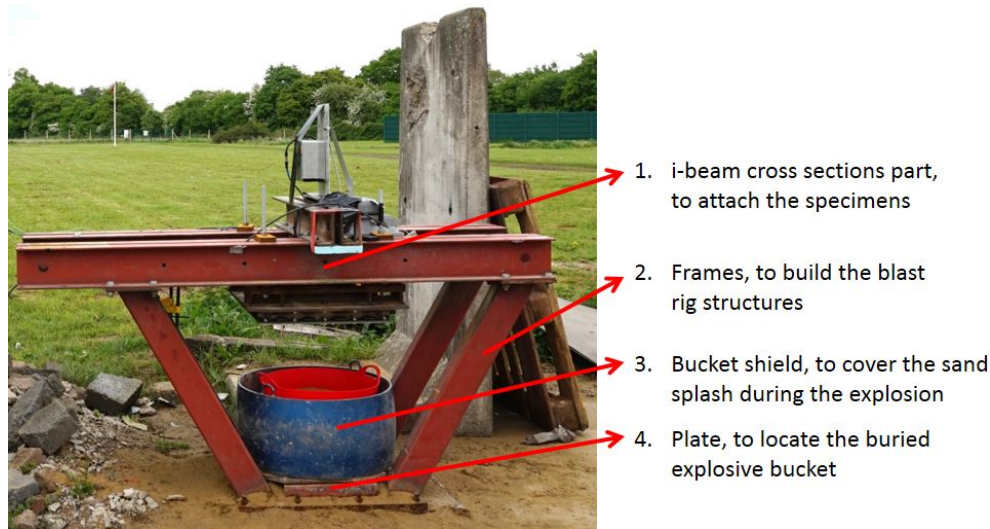
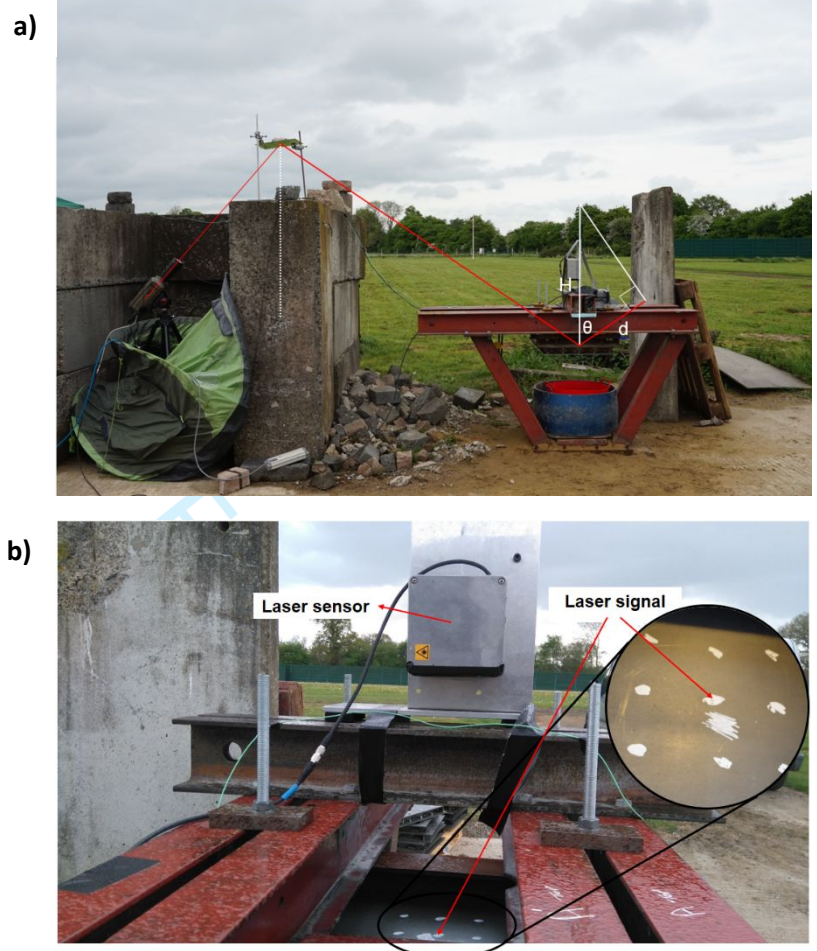


**Figure 7:** Instrumented blast rig instrument setup at the ERDA

Plate deflection was measured using two methods: a Keyence LK G507 displacement laser sensor and a high speed Phantom V12 camera. The laser sensor was positioned centrally above the test panel and had a set working range set at 0 to 100 mm, over a 10 V range. Data were sampled at 10 kHz and triggered by the piezo-electric pre-trigger. The laser signal instrument was installed on the blast rig perpendicularly at the middle point of the panel. The deflection was measured by pointing the laser signal and measuring the change of the laser length. Raw data from the laser signal was processed using point data average method to remove the noise as normalized data.

The High Speed Video (HSV) captured using Phantom V12 camera was located at a distance behind a Pendine block barricade and used a mirror to observe the plate surface at a 540 x 540 pixel resolution at 21,005 FPS (Figure 8a). The angle of incidence of the mirror reflection was corrected using the trigonometric relationship. A simple trigonometry concept determined the vertical plate displacement, where theta ( $\theta$ ) was measured to be 34°. For a high-speed camera, due to the perspective view change on the image, the horizontal distance of the white points was used. On the back face of the panels, white spots were marked in a 3x3 grid, spaced 50 mm apart to enable post-experimental displacement tracking using the Phantom Camera Control software (PCC) 2.6. The laser signal was directly aimed at the middle white spot (Figure 8b). As part of the tracking process, the PCC software requires a scale calibration to relate pixels to distance. For each video, scale calibration was taken about the horizontal axis, and measured between the centres of two 50 mm apart marks. Once calibrated, a tracking region was set. In all tests, the tracking region was set about the central mark as it remained within view until the detonation products and sand obscured the plate. A comprehensive method of how tracking works within PCC is detailed in <sup>73</sup>. Plate deflection measured using the Keyence LK G507 was measured centrally, and zeroed before each test to mitigate against pre-loading.

1  
2  
3  
4  
5  
6  
7  
8  
9  
10  
11  
12  
13  
14  
15  
16  
17  
18  
19  
20  
21  
22  
23  
24  
25  
26  
27  
28  
29  
30  
31  
32  
33  
34  
35  
36  
37  
38  
39  
40  
41  
42  
43  
44  
45  
46  
47  
48  
49  
50  
51  
52  
53  
54  
55  
56  
57  
58  
59  
60



278

279

**Figure 8:** a) Phantom V12 high-speed camera installation to record the central displacement of the panel. The camera captured by reflected the response by the mirror with theta,  $\theta$  is  $34^\circ$ ; b) The 5 mm apart white spots in 3 x 3 grid is used for V12 high speed camera processing through the PCC software to trace the displacement.

283

284

## 4. Result and Discussion

### 4.1. Negative Poisson's ratio behaviour

The auxetic core was compressed computationally to determine the bulk Poisson's ratio as a structural characteristic prior to experimental testing (Figure 9), where the greatest negative Poisson's ratio (-0.35) was shown to occur at the beginning of compression. At the initial condition, the cross-section of the auxetic panel is shown as a bow-tie structure in perfect shape without welding condition between the cellular walls. This shell element modelling was different from the real condition where the point welding used to join the bow-tie cellular. At 0.20 strain condition, the shrinkage arrangement to the centre direction started to appear. Next on 0.65 strain, the core panel became fully dense in the central region before it expanded and regained to the base material Poisson's ratio on 0.74 strain.

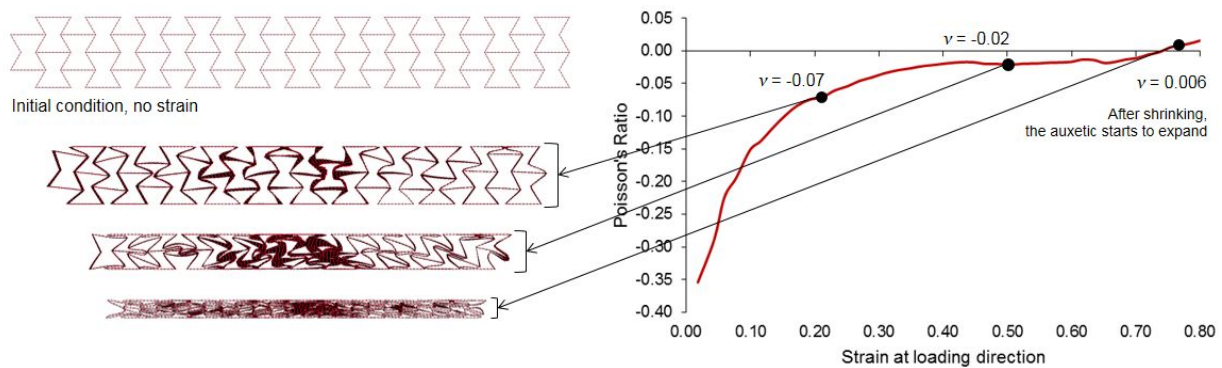
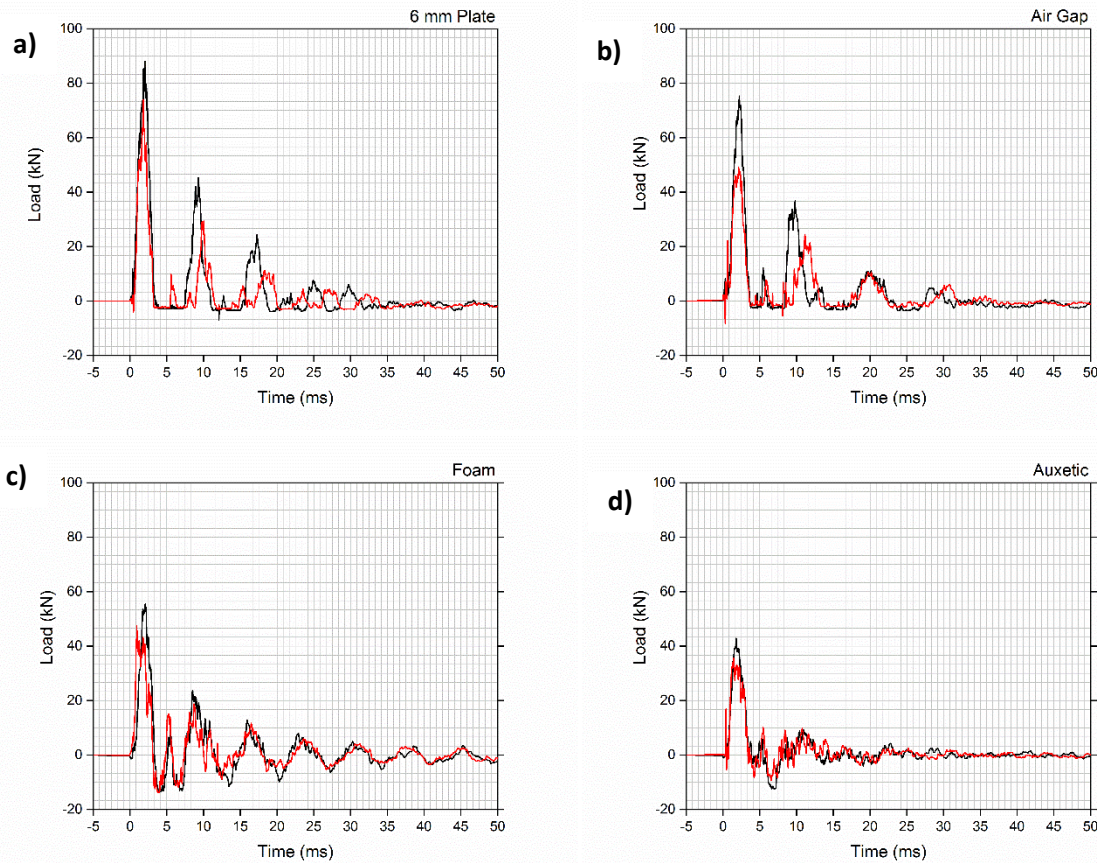


Figure 9: Compression modelling of the auxetic core with structural bulk Poisson's ratio detailed graphically relative to strain.

### 4.2. Impulse and blast loading

Figure 10 shows the average peak force-time profiles for the different panel configurations, with a summary of individual data given in Table 4. To mitigate experimental noise, a 5-point rolling average filter was applied to the raw force data.



**Figure 10:** Force-time profiles for a) 6mm Plate, b) Air Filled Panels, c) Foam filled Panels, and d) auxetic filled panels, for sensors S/N 389 (—) and S/N 625 (—)

**Table 4:** Experimental and numerical results of mean load and central transversal displacement

Configuration	Experimental Sample	Average Load S/N 389 (kN)	Average Load S/N 625 (kN)	Total impulse (kN.s)	Z displacement [back plate]			Z Displacement [face plate] (mm)
					Laser (mm)	Video (mm)	Model (mm)	
Monolithic	SS1	-	-	-	10.91	11.70	17.44	-
	SS2	-	-	-	13.33	9.84		
	SS3	-	-	-	25.32	14.72		
	SS4	84.47	67.84	494	14.19	13.98		
Air gap	SA1	57.21	-	-	-	10.78	15.64	48.78
	SA2	53.53	43.36	166	18.36	10.68		
	SA3	73.75	47.26	393	8.38	13.26		
Styrofoam core	SF1	59.35	46.25	302	25.67	-	7.3	53.1
	SF2	59.83	38.14	297	2.45	-		
	SF3	54.60	44.01	335	22.28	15.26		



<b>Auxetic core</b>	SX1	41.16	39.54	262	-	13.45	12.44	3.67
	SX2	41.58	34.82	246	20.87	-		
	SX3	66.34	55.94	251	16.68	-		
	SX4	66.34	55.94	257	13.16	10.46		

308

309 All experiments exhibited comparable force-time profiles, where a primary peak loading lasting between  
 310 2 to 3 ms in duration before transitioning to a negative load. As time progresses, a series of positive and  
 311 negative peaks repeat until full attenuation. The 6 mm plate data was the exception as no discernible  
 312 negative loading data is shown. The absence of negative loading, suggests that either the DAQ system is  
 313 cutting off data, or sensors were not fixed correctly. Unfortunately, it is difficult to clarify this, as unlike  
 314 the other profiles, only the data from the 6mm plate test 4 is presented in Figure 10, as DAQ failure  
 315 resulted in no usable data being recorded due to an over-ranging error. To ensure this behaviour did  
 316 not occur in later tests a 10:1 channel reducer was introduced.

317 Good correlation existed between the two sensors with the exception of the air-filled plates which were  
 318 particularly noisy. In most tests greater loading was experienced by sensor S/N 389, indicating an  
 319 irregular loading pattern. There are two potential sources for the irregular loading. One reason could be  
 320 due to support plate distortion induced from repeated exposure to the blast. This explanation however  
 321 fails to account for the lack of consistency throughout testing. A more likely explanation is the soil  
 322 ejecta impacting the plate is either anisotropic in impact location or in geometrical shape. For mediums  
 323 such as the sand, the loading at any discrete location is dictated by the particle size that impacts the  
 324 location and its momentum induced from the explosive charge<sup>58</sup>. This coupled with the variation in sand  
 325 humidity (detailed in Appendix A) makes for a more likely explanation. Unfortunately due to the location  
 326 of the high speed camera coupled with the blast products, the ability to observe loading pattern from  
 327 the ejecta was not observable within this study.

328 On average the monolithic samples exhibited the greatest peak loading of 84.47 kN, with auxetic  
 329 samples exhibiting the lowest at 41.16 kN. Generally, all panels were highly variable in similar range,  
 330 with error variance being approximately 14% for S/N 389 and 11% for S/N 625. Greater consistency was  
 331 shown for the foam cored panels with error variance approximately 3% and 4% of the mean for S/N 389  
 332 and S/N 625 sensors respectively. Assuming the 6 mm plate as the control, both the auxetic and foam  
 333 infills offer a mean loading and impulse mitigation of 33% and 34% respectively. Alternatively, the air  
 334 filled panels have the potential to both amplify and mitigate the pressure and impulse experienced.

335 In a series of tests a low intensity, rapid loading event occurred prior to first peak without bias across  
 336 panel configurations. Such behaviour has been previously reported by Ramasamy et al.<sup>74</sup>, and is  
 337 referred to as the detached shock wave. While this interaction induces a loading effect on the plate,  
 338 due to acoustic impedance between the sand and air, only a small fraction of the incident shock is  
 339 transmitted into the air, causing the resultant air shock to have minimal influence on the target  
 340 structure<sup>75</sup>. Instead, the initial peak loading is caused by the soil ejecta. According to Deshpande et al.  
 341<sup>76</sup> and Børvik<sup>77</sup> up to two thirds of the impulse is delivered to a vehicle is from the soil ejecta, with the  
 342 remaining third delivered by the blast products.

343 While the fixed conditions of testing coupled with the test data, can allow for the assumption that they  
 344 are induced by the blast products and soil ejecta, it fails to account for the irregular subsequent data

peaks trends such as, the third peaks always being lower than the fourth. It is postulated that this behaviour could be caused by the presence of a reflected wave between the rig and the panel during the loading event. Alternatively, it could be caused by the fluttering or vibration response of the structure induced from the blast impact. The flutter occurred in an oscillation trend between the peaks. Frequencies were calculated from the period between the peaks and were found to be approximately 1282 Hz, 1338 Hz, 1000 Hz, 1420 Hz, for monolithic, air gap, foam, and auxetic respectively. We compared with the numerical analysis and found out that the 6<sup>th</sup> mode of monolithic damped frequency is 1194 Hz. The numerical result strengthens the argument that it could be a damped oscillation. It is consistent also with dynamics principles where stiffer the panel, higher the frequency mode would be.

When considered in the impulse domain the auxetic panels exhibited the lowest mean impulse while the monolithics exhibited the most (**Figure 11**). The single 6mm plates were comparable to the air plates in measured impulse, while the foam infills were more comparable to the auxetic panels. Once again the air-filled panels were highly variable with error variance being approximately 57.43% of the mean, while foam and auxetic panel configurations were fairly consistent with an average error of 6.63% and 2.75% of the mean respectively. Although unclear why the air-filled panels demonstrated such large variation, it is suspected that it is caused by the high pressure experienced at sensor S/N 39 in test SA3. Although the cause of this high pressure is difficult to ascertain, the variance indicates that the soil ejecta that interacts with the plate is either anisotropic in impact location or in geometrical shape. For mediums such as the sand used in this study, the experienced loading at any discrete location is dictated by the particle size at that location and its momentum induced from the explosive charge<sup>78</sup>. This is further supported by the wider literature where soil type and charge shape are reported to be the principle parameters that influence loading<sup>75,79-85</sup>. As such if some part of the soil ejecta impacted directly at the sensor location, a greater loading and subsequent impulse would be recorded. Unfortunately with only two data points (both significantly different), it is difficult to validate this theory.

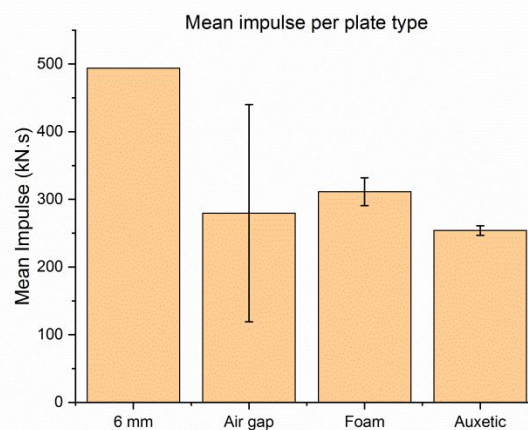


**Figure 11:** Mean impulse per panel type where errors represent standard deviation

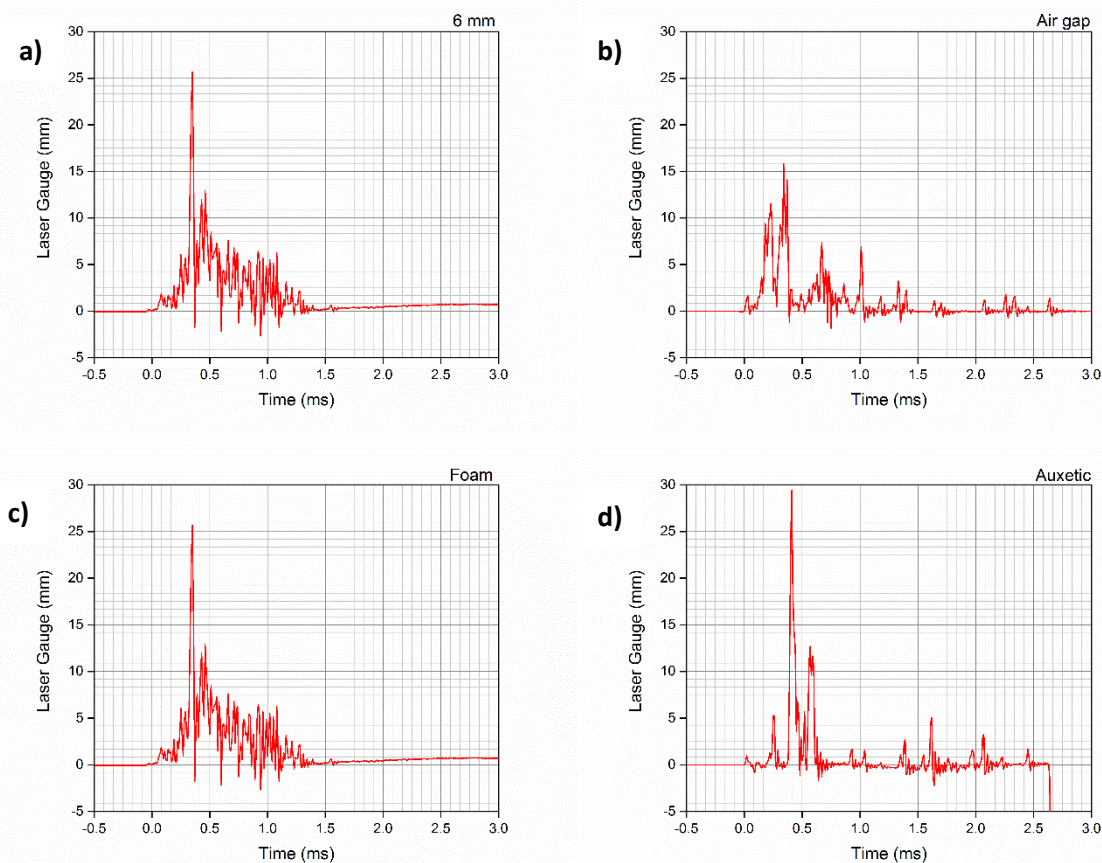
In this study, the non-dimensional parameters did not fulfil the requirements. All variables were input in the equation and compared both results of total impulse in the MATLAB and LS-DYNA. Both the MATLAB and LS-DYNA models yielded comparable results of 649 and 650 kN.s, respectively. Even though the 15% reduction is a range between the intervals of 1.8 factor, this reduction is caused by the non-fulfilment of

375 the parameter limitations required. However, by scaling down the total impulse in LS-DYNA, the  
 376 numerical results were expected to show similar deflection compared to the experimental observation.

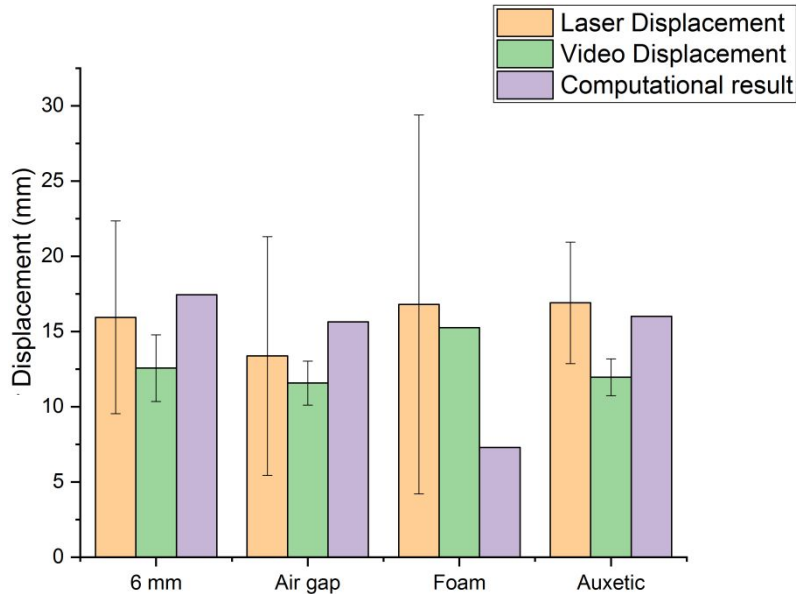
377 By scaling down the total impulse in the simulation setup, the simulation showed expected results with  
 378 similar deflection compared to the experimental observation, as shown in the next sub-section. The  
 379 mean impulse for all panels, excluding 6mm was approximately 300 kN.s. Solving Tremblay to calculate  
 380 the vertical impulse of buried mine <sup>54</sup> using the experimental parameters herein, an impulse of 650 kN.s  
 381 was produced; a value significantly different than the observed result. It is suspected that the deviation  
 382 between experimental and calculated value as the parameter criteria did not fulfil the Tremblay function  
 383 limitation, as detailed in Table 1. In light of this, the mean impulse value for each panel configuration  
 384 was used in the numerical analysis by scaling the impulse to replicate the actual deflection response.

### 385 4.3. Deflection response

386 **Figure 12** shows an example of deflection-time profiles recorded by the laser. Noise was removed 5-point  
 387 rolling average filter and normalized about the zero. Mean maximum deflection data the laser system  
 388 and HSV is provided in **Figure 13**.



391 **Figure 12:** Deflection-time profile based on the laser signal result for a) 6mm Plate, b) Air Filled Panels, c) Foam  
 392 filled Panels and d) auxetic filled panels



394  
395 **Figure 13:** Mid-point displacement of the panels: experimental vs numerical result. Laser system provides physical  
396 location measurement (panel displacement) during testing to provide comparison to secondary measurement  
397 from HSV and provide validation to computational model.

398  
399 The air filled panels exhibited the lowest displacement, followed by the 6mm, foam, and auxetic  
400 respectively. Similarly the laser system, HSV indicated that the lowest mean displacement was exhibited  
401 by the air panels, followed by auxetic, 6mm, and foam infills respectively.

402 All instances, HSV recorded consistently a smaller displacement than the laser by up to 29%. Both  
403 systems were considerably variable with error (given by standard deviation) ranging from 23% to 75%  
404 and 10% to 17% of the mean displacement for the laser system and HSV respectively. The maximum  
405 deflection occurs at the interval between 0.5 – 1 ms on all panels. Both systems were relatively  
406 comparable with mean deflections recorded between 13 mm to 27 mm, and 11 mm to 15 mm being  
407 recorded for the laser system and HSV respectively.

408 Analysis of the temporal dominion found that displacement occurred between a mean duration of  $2.0 \pm$   
409  $0.6$  ms and  $3.6 \pm 0.65$  ms for the laser system and HSV, respectively (**Figure 14**). Interestingly, the laser  
410 system showed that as the panels went from a single panel, to a more composite panel, the  
411 displacement duration decreased, with the auxetic panels being the lowest. Alternatively, the HSV  
412 presents that changing from a single plate to a composite panel the displacement duration either  
413 increases (air filled and auxetic core) or remains comparable.

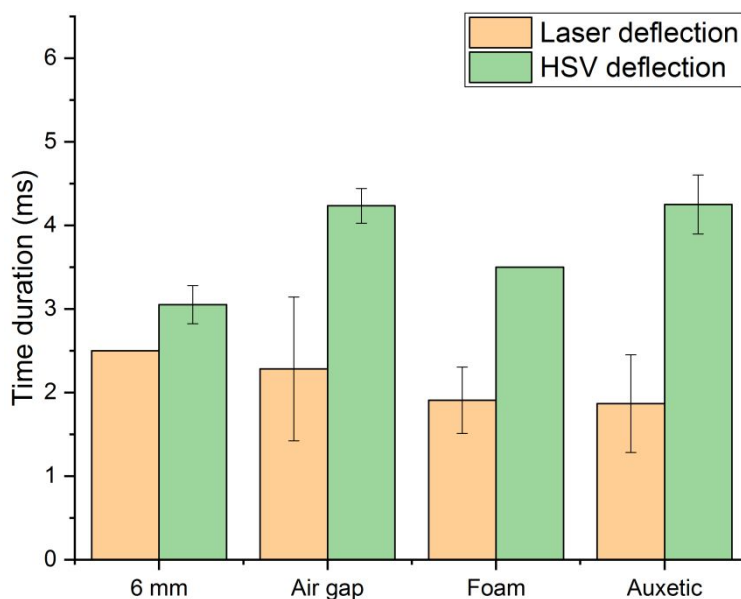


**Figure 14:** Time duration of displacement per panel type using laser system and HSV

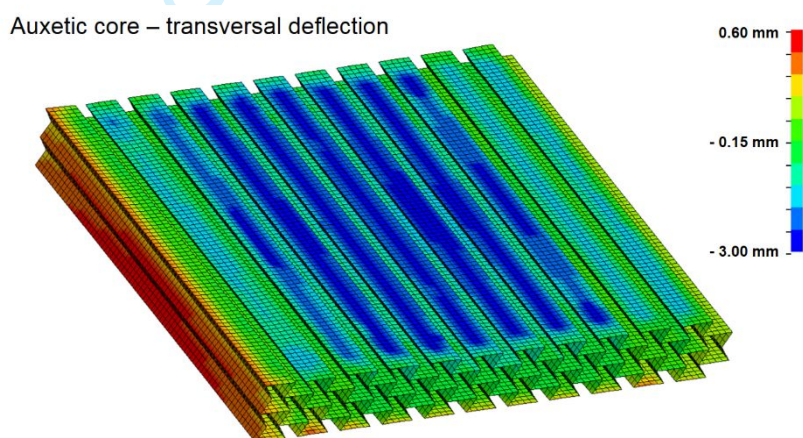
Interestingly stand deviation between panels was also shown to be influenced by measurement technique. The laser system reported a more broad range of variance from 8% to 32%, while the video had a variance of 1% to 3% of the mean displacement mean duration respectively. The differences between measured displacements are likely due to a number of factors, the most influence being location of the sensing system. In the case of the HSV, the camera was protected from the majority of the blast effects by the Pendine wall allowing for a continued observation of the event. While interactions of the blast products on the mirror are likely to play a role, the low error between datasets suggests that its influence is likely minimal. On the contrary, the laser system was directly located above the panel system and was more subjected to the blast products, as evident by the many dislocation of the laser system post explosive tests. Data capture rate is also likely to play a role in the fidelity of the data, however the influence of such factor is not considered herein.

When compared against the models (**Figure 13** and **Table 4**), the difference between maximum model deflections and the mean panel deflections recorded by laser system and the HSV were -56% to 16% and -52% to 38% respectively, with the biggest deviation exhibited by the foam filled panels. These deviations are likely caused by a coupling of idealised conditions induced through computer modelling along with assumptions and simplifications made within material modelling. For example instead of developing the smooth negative exponential of stress-strain function, a plastic kinematic material model was used which only generates a trapezoidal function<sup>55</sup>. This simplification may also account large deviation observed between the foam experimental and numerical results. Unlike in the experimental where the foam would be compressed and compact until densification, the model did not replicate the densification effect.

During the densification, the modulus is drastically changed from the sloping plateau to the steep second modulus. However, in the numerical, the foam material absorbed the impact energy by shrinking the element. This stage worked in stress plateau region. After that, the second modulus is input similarly with the first elastic modulus due to the lack of true stress-strain data. It contributes to reduce the

441 deflection of back plate because we assume that the foam core would still absorb the energy in  
 442 densification region, instead of loading the back plate. It is also suspected that the application of using a  
 443 deletion mechanism on the foam element when it has reached the failure stress due to the pressure  
 444 traveling from the face plate, where in reality the foam would continue to load the back plate.

445 A notable deviation was also observed for the auxetic panel where it was found that 160 grams of PE4  
 446 failed to initiate re-entrant behaviour to absorb the energy, although some transversal deflection did  
 447 occur (**Figure 15**). Without being able to observe the auxetic core loading and deflection during the  
 448 explosive event, it is difficult to confirm if this behaviour was isolated to the model or indicative of real  
 449 world behaviour. Interestingly post impact there was evident of damage to the auxetic core in the way  
 450 spot weld failure between the auxetic cells (**Figure 16**), and is likely one of the principle mechanisms of  
 451 blast load absorption. This behaviour failed to be replicated in the auxetic model as the spot welding  
 452 was not modelled, and thus could influence the model response as it did not have natural failure  
 453 locations.



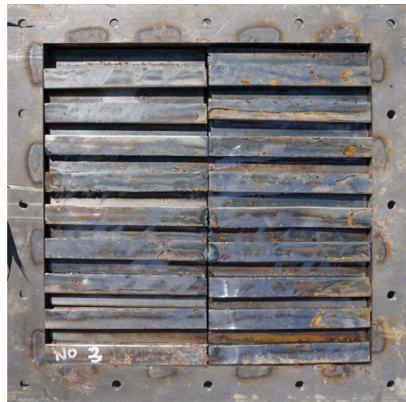
455

456 **Figure 15:** The transversal deflection profile of auxetic core at 0.9 ms. The face part shows the higher deflection  
 457 due to the first momentum transfer directly from the face plate

458 The auxetic model also saw the back plate deflect further than the face plate due to several possibilities.  
 459 The absence of adhesive between each plate could oscillate each layer during the explosion and also the  
 460 mechanism of absorption of explosive energy that could be mistaken. We assume that the stiffness of  
 461 the same thickness face plate and back plate is the cause. The 3 mm panel configuration on the top and  
 462 bottom behaves like a solid structure and only transfer the loading from the front to the bottom.  
 463 Whereas the face plate should have been the first side to be hit by the sand ejecta, then the loading was  
 464 transferred to the core so that the auxetic shrink. This shrinkage behaviour should be an absorbent of  
 465 impact energy so that deflection can be reduced at the back of the plate. This result may be different if  
 466 the back plate that is on the inside has a thicker size or vice versa, the face plate is thinner.

467 Other notable damage to occur throughout testing was the presence of denting on the front panels  
 468 (**Figure 17**). While every effort was taken to ensure the sand was levelled prior to testing, the spread of  
 469 denting indicates that either the soil ejecta didn't load uniformly or that clumping occurred. This non  
 470 uniform loading could explain the variance in each panel configuration as shown in **Table 4**.

471



Auxetic panel, post-explosion.  
No visible deformation at the core.



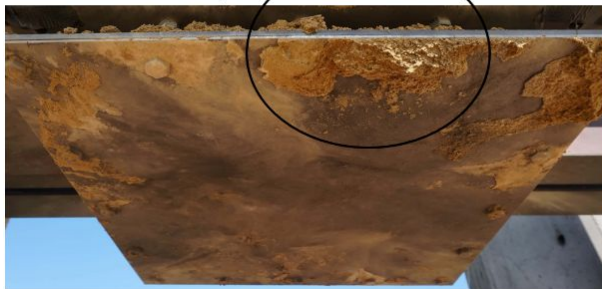
Auxetic core, post-explosion.  
The welding were broken and the auxetic did not perform an effective negative Poisson's ratio to absorb the impact energy.

472

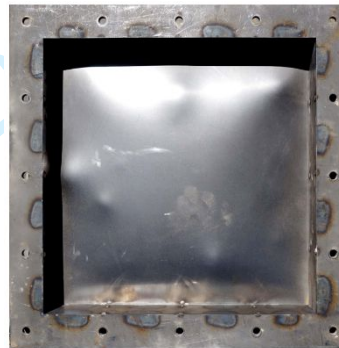
473 **Figure 16.** Auxetic sandwich panel post-test condition highlighting weld failure and compression of the  
474 lattice structure.

a)

Even after sifted the sand  
before used, the lump sand  
were found at some local points



b)



Dents were found in the air gap  
panels (face plate).  
It is confirmed that the face section  
was plastic deformed.  
Moreover, the dents showed that  
the sand ejecta was not uniform

475

476 **Figure 17.** Dent damage observed on a) front panel for monolithic and air gap panels, highlighting  
477 potential non-uniform sand ejecta, and b) rear panel.

#### 478 4.4. Panel response with respect to panel mass

479 **Figure 18** shows the plot comparison per panel against mass for maximum force, impulse and deflection.  
480 The mass of panel type were approximately 7.5 kg, 7.5 kg, 7.8 kg, and 18.7 kg for 6 mm panel, air filled,  
481 foam core and auxetic, respectively.

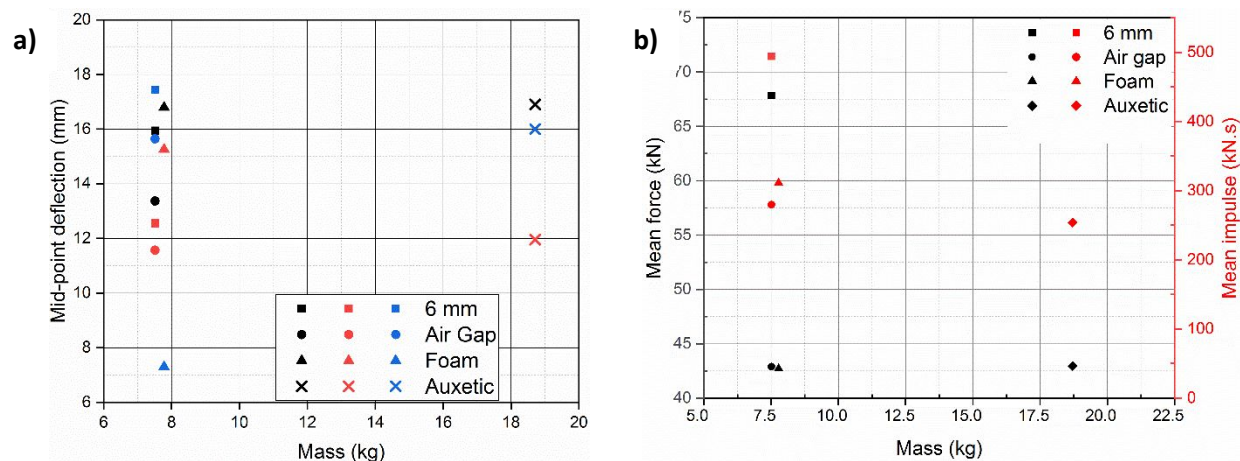


**Figure 18:** a) Maximum deflection per panel type against mass; black = laser deflection, red = HSV deflection, blue = simulation deflection, b) Mean force and mean impulse per panel type against mass

As presented in Figure 16 a), comparison of each of the deflection measurements (i.e. laser system, HSV, and numerical modelling) found that foam panels were predicted to be the most effective, with the air filled experimental panels being the most efficient per unit mass. Alternatively the, auxetic core was comparable to the other systems in deflection behaviour but at a significant mass increase, making it an unfavourable strategy to deter the blast loading due to several reasons. Furthermore, Figure 16 b) shows that the mean force and mean impulse against mass equal to the deflection response. The air filled panel could absorb the energy by deformed the face plate and reduced the received force and impulse in the back plate. By against it mass, the air filled panel is seen the most effective to deter 160 gram PE4 because due to the graph, that the response mean impulse and mean force of air filled panel placed in the most left and corner which means that the air filled is the least weight with the most effective in response. Contrary the auxetic core panel was under performed, even when normalized by the mass. The auxetic filled panel could absorb the impact energy and reduce the mean force and impulse, however by normalizing it by its mass makes the panel is heavier compared to the other panels.

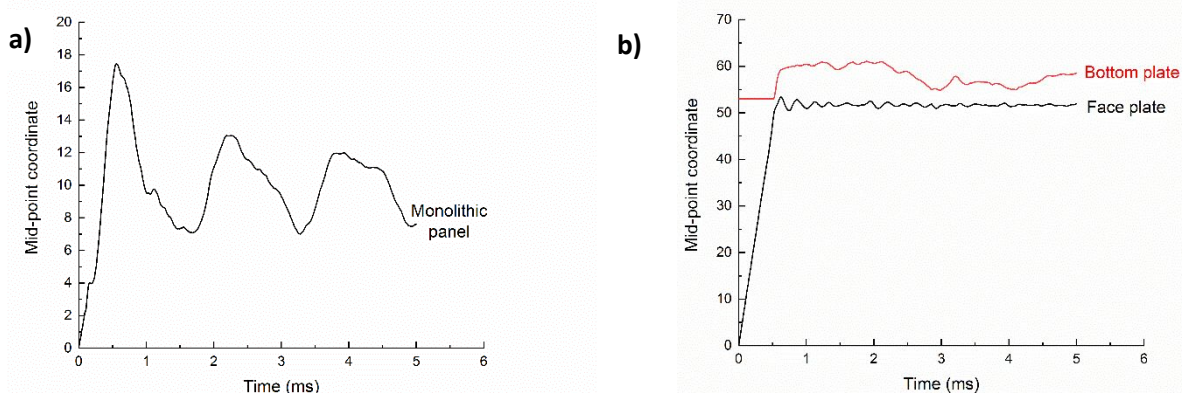
Furthermore, we found the effect of sand humidity is not that sensitive in this study. As presented in Table A that the sand humidity recorded in the charge location of auxetic core panel test 4 is a slightly dense than other, approximately 46% below the PE4 charge, even the surrounding humidity is relatively similar for each test. The moister sand could not increase the explosion momentum. It is noticed that the recorded momentum in SX4 test and the other auxetic tested panels with lower humidity are not far different. Rather, we presume that the momentum transfer mechanism through the panel core could determine the panel response.

In monolithic plates, the incoming shock wave imparts a velocity only to the face plate. The face plate is accelerated in responses to the impulse loading. The face plate would deform and vibrate to dissipate the energy. Meanwhile, in sandwich panels, the face panel would meet the core. The face panel immediately decelerated whilst the core and rear panel are accelerated. The energy lost is assumed as a dissipated energy due to the panel deformation or core compression<sup>86</sup>. In air filled panels the face plate would receive a transfer momentum from the shock wave of buried charge. The face plate would be displaced and deformed until 5 mm before contact with the back plate. The energy is dissipated as plastic deformation of face plate before impact the back plate. In foam filled panel, impact energy is



513 dissipated into three components, i.e. face plate, solid foam, and back plate. Similarly with the foam  
 514 filled, auxetic core panel will absorb the energy by three components, i.e. face plate, auxetic core, and  
 515 back plate.

516 The authors are unclear why the sandwich panels do not exhibit the presumption performance. The  
 517 relatively similar deflection could be caused by (i) the momentum transfer is insufficient to cause  
 518 permanent displacement of the back plate and (ii) the layer at each panel behave independently  
 519 because there is no bonding between them. Interestingly in <sup>51</sup>, it was reported that there is a tendency  
 520 with the 500 mm stand-off distance and 208 grams of TNT equivalent mass that the single panel is  
 521 deflected relatively comparable with the sandwich configurations. This could be caused by the elastic  
 522 behaviour of the panel. Moreover, related to the insufficient of loading impulse, the panel would  
 523 displace independently instead of move together as a one sandwich panel as seen in **Figure 19**. In Figure  
 524 17 a), the trace of mid-point of monolithic is presented. The single point move freely, there is no  
 525 momentum transfer, thus the panel would absorb the energy by a single plate. Meanwhile, Figure 17 b),  
 526 c), d) shows a mid-point trace in the sandwich panels. In those panels, the momentum transfer occurred  
 527 at the moment of impact between the layers. The air filled panels in Figure 17 b) shows a momentum  
 528 transfer between the face and bottom plates. The face plate was plastically deformed until it reaches  
 529 the bottom plate surface. It pushed the bottom plate and then the face plate was pushed back to  
 530 forward direction and vibrated. In Figure 17 c) the trace of mid-point of foam filled panel was displayed.  
 531 It can be observed that there is a delay between the first and the second momentum transfer. The first  
 532 momentum transfer occurred at approximately 0.1 ms made the face plate and the top surface of the  
 533 foam collided each other, while the second momentum occurred slightly after it at approximately 0.5  
 534 ms. Figure 17 d) shows the mid-point trace of auxetic core panels. The momentum transfer between  
 535 the layers occurred almost at the same time, approximately at 0.45 ms. However, as stated before that  
 536 it can be seen there is similarity mechanism between the sandwich panels that the plates of the panels  
 537 deflected independently. At some time, the layers moved far apart at the momentum transfer.  
 538 Meanwhile, at the other time they moved closer and impact occurred, the plates damped each other's  
 539 movements.



540

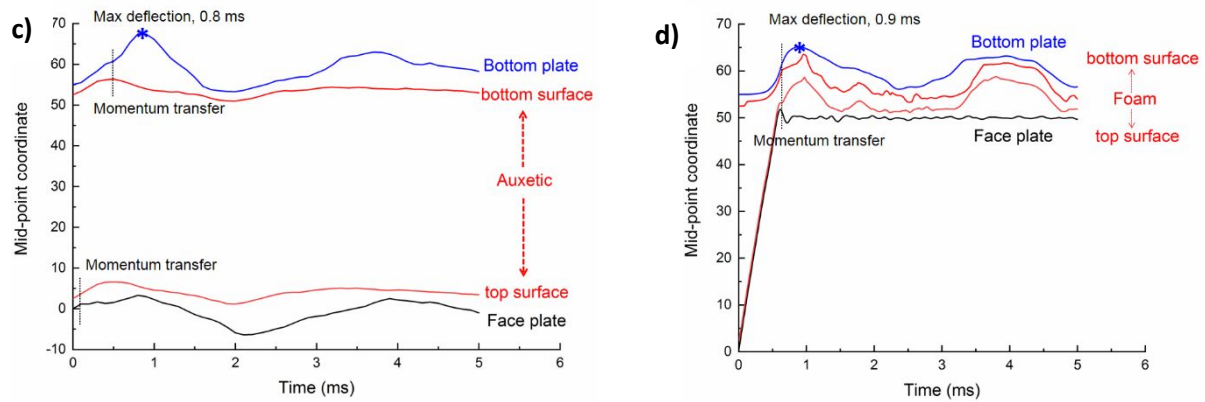


**Figure 19:** Mid-point momentum co-ordinate profile during explosion in transversal axis (z) for a) monolithic, b) air, c) foam and d) auxetic panels.

In auxetic core panels, at the time of momentum transferred the core plate would be accelerated and hit the back plate. At this stage, the core plate was decelerated and the back plate is accelerated. The plates behave independently because they are not tied by an adhesive or plastic deformation, thus the transferred momentum push the back plate and deflect it. It is possible to exhibit the comparable displacement between the auxetic and monolithic panel because the mass of back plate of auxetic panel is only 3 mm CR4 steel which is less than 6 mm monolithic panel (The 3 mm panel could have plastic deformation and hit the 50 mm back plate in air filled panel). Thus, the remaining energy of transferred momentum in back plate is still capable to deflect it until 11 to 16 mm.

In addition, it is also unclear that the dissipated energy of the compressed foam core could not damp the back plate in foam panels. We assume that the same transferred momentum mechanism occurred in the foam filled panels.

## 5. Conclusions

Auxetic and foam core panels are a promising structure against buried mines, as they demonstrated a lower loading response compared to the monolithic panels of the same material. Deflection measurements were highly variable throughout testing, with the laser system reporting errors as great as 75%; a behaviour likely caused by its near location to the blast event. Nonetheless the air filled panels were the most promising at minimising rear plate deflection as confirmed by all three methods (HSV, laser system and computational modelling). Numerical modelling provided a good prediction of the plate deflections responses with some variation, which were likely caused by the simplified material models employed. Once normalised against panel weight, to understand how mass efficient each system was, the air filled panels were experimentally the most efficient per unit mass, with the auxetic core being the least effective.

## Acknowledgement

We would particularly like to thank to ERDA officers and Cranfield Workshops, especially Karl Norris, and Chris Williams for the manufacturing of the samples. The authors would also like to thank Mike Teagle,

1  
2  
3 570 Dave Miller and Alan Peare for their assistance during testing and ensuring trouble free data collection.  
4 571 Lastly we would like to thanks LSTC for providing the on LS-DYNA academic license to undertake the  
5 572 computational modelling element of this work.  
6  
7  
8  
9  
10  
11  
12  
13  
14  
15  
16  
17  
18  
19  
20  
21  
22  
23  
24  
25  
26  
27  
28  
29  
30  
31  
32  
33  
34  
35  
36  
37  
38  
39  
40  
41  
42  
43  
44  
45  
46  
47  
48  
49  
50  
51  
52  
53  
54  
55  
56  
57  
58  
59  
60

For Peer Review

573 **References**

- 574 1. Bird R. Protection of Vehicles Against Landmines. *J Battlef Technol*; 4.
- 575 2. NATO (North Atlantic Treaty Organisation). *STANAG 4659: Protection Levels for Occupant of*  
576 *Armoured Vehicles*. 2012.
- 577 3. NATO (North Atlantic Treaty Organisation). *AEP-55 'Procedures for Evaluating the Protection*  
578 *Level of Armoured Vehicles - Mine Threat'*. 2011.
- 579 4. Mann CT, Fischer H. *Recent Trends in Active-Duty Military Deaths Non-OCO Deaths*,  
580 <https://fas.org/sgp/crs/natsec/IF10899.pdf> (accessed 30 October 2018).
- 581 5. Schneck W. *The Development of Mine Resistant Vehicles*. Virginia, USA, 1994.
- 582 6. Hazell PJ. *Armour: Materials, Theory, and Design*. CRC Press, 2016.
- 583 7. Chun Hong Kelvin Yap. *The impact of armor on the design, utilization and survivability of ground*  
584 *vehicles: the history of armor development and use*. 2012.
- 585 8. Donoghue JP, Alderson KL, Evans KE. The fracture toughness of composite laminates with a  
586 negative Poisson's ratio. *Phys Status Solidi Basic Res Res* 2009; 246: 2011–2017.
- 587 9. Qin H, Sun Y, Liu JZ, et al. Negative Poisson's ratio in rippled graphene. *Nanoscale* 2017; 9: 4135–  
588 4142.
- 589 10. Li T, Chen Y, Wang L. Enhanced fracture toughness in architected interpenetrating phase  
590 composites by 3D printing. *Compos Sci Technol* 2018; 167: 251–259.
- 591 11. McDonald SA, Dedreuil-Monet G, Yao YT, et al. In situ 3D X-ray microtomography study  
592 comparing auxetic and non-auxetic polymeric foams under tension. *Phys Status Solidi Basic Res*  
593 2011; 248: 45–51.
- 594 12. Choi JB, Lakes RS. Nonlinear properties of polymer cellular materials with a negative Poisson's  
595 ratio. *J Mater Sci* 1992; 27: 4678–4648.
- 596 13. Jin S, Korkolis YP, Li Y. Shear resistance of an auxetic chiral mechanical metamaterial. *Int J Solids*  
597 *Struct* 2019; 174–175: 28–37.
- 598 14. Lorato A, Innocenti P, Scarpa F, et al. The transverse elastic properties of chiral honeycombs.  
599 *Compos Sci Technol* 2010; 70: 1057–1063.
- 600 15. Li D, Dong L, Lakes RS. The properties of copper foams with negative Poisson's ratio via resonant  
601 ultrasound spectroscopy. *Phys Status Solidi Basic Res* 2013; 250: 1983–1987.
- 602 16. Cheng H, Wang F, Bian Y, et al. Co- and self-activated synthesis of tailored multimodal porous  
603 carbons for solid-phase microextraction of chlorobenzenes and polychlorinated biphenyls. *J*  
604 *Chromatogr A* 2019; 1585: 1–9.
- 605 17. Chen CP, Lakes RS. Micromechanical analysis of dynamic behavior of conventional and negative  
606 Poisson's ratio foams. *J Eng Mater Technol* 1996; 288: 285–288.
- 607 18. Duc ND, Cong PH. Nonlinear dynamic response and vibration of sandwich composite plates with  
608 negative Poisson's ratio in auxetic honeycombs. *J Sandw Struct Mater* 2016; 20: 692–717.

- 1  
2  
3 609 19. Dinh N, Seung-eock K, Hong P, et al. Dynamic response and vibration of composite double curved  
4 610 shallow shells with negative Poisson's ratio in auxetic honeycombs core layer on elastic  
5 611 foundations subjected to blast and damping loads. *Int J Mech Sci* 2017; 133: 504–512.
- 7 612 20. Critchley R, Corni I, Wharton JA, et al. A review of the manufacture, mechanical properties and  
8 613 potential applications of auxetic foams. *Phys Status Solidi Basic Res* 2013; 250: 1963–1982.
- 10 614 21. Alderson KL, Fitzgerald A, Evans KE. The strain dependent indentation resilience of auxetic  
11 615 microporous polyethylene. *J Mater Sci* 2000; 35: 4039–4047.
- 13 616 22. Argatov II, Guinovart-Díaz R, Sabina FJ. On local indentation and impact compliance of isotropic  
14 617 auxetic materials from the continuum mechanics viewpoint. *Int J Eng Sci* 2012; 54: 42–57.
- 16 618 23. Hu LL, Zhou MZ, Deng H. Dynamic indentation of auxetic and non-auxetic honeycombs under  
17 619 large deformation. *Compos Struct* 2019; 207: 323–330.
- 19 620 24. Dai Z, Weng C, Liu L, et al. Multifunctional Polymer-Based Graphene Foams with Buckled  
20 621 Structure and Negative Poisson's Ratio. *Sci Rep* 2016; 6: 1–9.
- 22 622 25. Yu L, Yan Q, Ruzsinszky A. Negative Poisson's ratio in 1T-type crystalline two-dimensional  
23 623 transition metal dichalcogenides. *Nat Commun* 2017; 8: 1–8.
- 24 624 26. Lantada AD, De Blas Romero A, Schwentenwein M, et al. Lithography-based ceramic manufacture  
25 625 (LCM) of auxetic structures: Present capabilities and challenges. *Smart Mater Struct*; 25. Epub  
26 626 ahead of print 2016. DOI: 10.1088/0964-1726/25/5/054015.
- 28 627 27. Hou J, Deng B, Zhu H, et al. Magic auxeticity angle of graphene. *Carbon N Y* 2019; 149: 350–354.
- 30 628 28. Liu G, Zeng Q, Zhu P, et al. Negative Poisson's ratio in monolayer PdSe<sub>2</sub>. *Comput Mater Sci* 2019;  
31 629 160: 309–314.
- 33 630 29. Zhang GH, Ghita O, Evans KE. The fabrication and mechanical properties of a novel 3-component  
34 631 auxetic structure for composites. *Compos Sci Technol* 2015; 117: 257–267.
- 36 632 30. Zhou L, Jiang L, Hu H. Auxetic composites made of 3D textile structure and polyurethane foam.  
37 633 *Phys Status Solidi Basic Res* 2016; 253: 1331–1341.
- 39 634 31. Alderson K, Nazaré S, Alderson A. Large-scale extrusion of auxetic polypropylene fibre. *Phys*  
40 635 *Status Solidi Basic Res* 2016; 253: 1279–1287.
- 42 636 32. Domaschke S, Morel A, Fortunato G, et al. Random auxetics from buckling fibre networks. *Nat*  
43 637 *Commun* 2019; 10: 1–8.
- 45 638 33. Jiang JW, Park HS. Negative poisson's ratio in single-layer black phosphorus. *Nat Commun* 2014;  
46 639 5: 1–7.
- 48 640 34. Dusfour G, LeFloc'h S, Cañadas P, et al. Heterogeneous mechanical hyperelastic behavior in the  
49 641 porcine annulus fibrosus explained by fiber orientation: An experimental and numerical  
50 642 approach. *J Mech Behav Biomed Mater*; 104. Epub ahead of print 2020. DOI:  
51 643 10.1016/j.jmbbm.2020.103672.
- 53 644 35. Underhill RS. Defence applications of auxetic materials. *DSIAC J* 2014; 1: 7–13.
- 55 645 36. Sun Y, Xu W, Wei W, et al. Stab-resistance of auxetic weft-knitted fabric with Kevlar fibers at  
56 646 quasi-static loading. *J Ind Text* 2019; 1–13.

- 1  
2  
3 647 37. Novak N, Starčević L, Vesenjāk M, et al. Blast response study of the sandwich composite panels  
4 648 with 3D chiral auxetic core. *Compos Struct* 2019; 210: 167–178.
- 6 649 38. Imbalzano G, Linforth S, Ngo TD, et al. Blast resistance of auxetic and honeycomb sandwich  
7 650 panels: Comparisons and parametric designs. *Compos Struct* 2018; 183: 242–261.
- 9 651 39. Qi C, Remennikov A, Pei LZ, et al. Impact and close-in blast response of auxetic honeycomb-cored  
10 652 sandwich panels: Experimental tests and numerical simulations. *Compos Struct* 2017; 180: 161–  
11 653 178.
- 13 654 40. Imbalzano G, Tran P, Ngo TD, et al. Three-dimensional modelling of auxetic sandwich panels for  
14 655 localised impact resistance. *J Sandw Struct Mater* 2017; 19: 291–316.
- 16 656 41. Imbalzano G, Tran P, Ngo TD, et al. A numerical study of auxetic composite panels under blast  
17 657 loadings. *Compos Struct* 2016; 135: 339–352.
- 19 658 42. Schenk M, Guest SD, McShane GJ. Novel stacked folded cores for blast-resistant sandwich beams.  
20 659 *Int J Solids Struct* 2014; 51: 4196–4214.
- 22 660 43. Jin X, Wang Z, Ning J, et al. Dynamic response of sandwich structures with graded auxetic  
23 661 honeycomb cores under blast loading. *Compos Part B Eng* 2016; 106: 206–217.
- 25 662 44. Bai X, Zhu L, Yu TX. Saturated impulse for pulse-loaded rectangular plates with various boundary  
26 663 conditions. *Thin-Walled Struct* 2017; 119: 166–177.
- 28 664 45. Cheng Y, Liu M, Zhang P, et al. The effects of foam filling on the dynamic response of metallic  
29 665 corrugated core sandwich panel under air blast loading – Experimental investigations. *Int J Mech*  
30 666 *Sci* 2018; 145: 378–388.
- 32 667 46. Boasberg J, The Department of Education, Academy T, et al. No 主観的健康感を中心とした在  
33 668 宅高齢者における 健康関連指標に関する共分散構造分析Title. *Duke Law J* 2019; 1: 1–13.
- 35 669 47. Yuen SCK, Nurick GN. Experimental and numerical studies on the response of quadrangular  
36 670 stiffened plates. Part I: Subjected to uniform blast load. *Int J Impact Eng* 2005; 31: 55–83.
- 38 671 48. Langdon GS, Yuen SCK, Nurick GN. Experimental and numerical studies on the response of  
39 672 quadrangular stiffened plates. Part II: Localised blast loading. *Int J Impact Eng* 2005; 31: 85–111.
- 41 673 49. Pickering EG, Yuen SCK, Nurick GN, et al. The response of quadrangular plates to buried charges.  
42 674 *Int J Impact Eng* 2012; 49: 103–114.
- 44 675 50. Schwer L, Teng H, Souli M. LS-DYNA Air Blast Techniques : Comparisons with Experiments for  
45 676 Close-in Charges. In: *10th European LS-DYNA Conference 2015*. 2015.
- 47 677 51. Holloman RL, Deshpande V, Wadley HNG. Impulse transfer during sand impact with a cellular  
48 678 structure. *Int J Impact Eng* 2015; 82: 36–58.
- 50 679 52. Fleck NA, Deshpande VS. The Resistance of Clamped Sandwich Beams to Shock Loading. 71. Epub  
51 680 ahead of print 2004. DOI: 10.1115/1.1629109.
- 53 681 53. Hutchinson JW, Xue Z. Metal sandwich plates optimized for pressure impulses. *Int J Mech Sci*  
54 682 2005; 47: 545–569.
- 56 683 54. Tremblay JE, Delagrave R. *Impulse on blast deflectors from a landmine explosion*. Valcartier,  
57 684 Quebec: Defence research establishment. 1998.

- 1  
2  
3 685 55. Hallquist JO. *LS-DYNA Theory manual*. 2006.
- 4  
5 686 56. Schwer L, Slavik T. Buried charge engineering model: verification and validation. In: *9th European*  
6 687 *LS-DYNA Conference 2013*. DYNAore GmbH, 2013.
- 7  
8 688 57. LSTC. *LS-DYNA: Keywords User's Manual I*.
- 9  
10 689 58. Bogosian D, Yokota M, Rigby S. TNT equivalence of C-4 and PE4: A review of traditional sources  
11 690 and recent data. *24th Int Symp Mil Asp Blast Shock (MABS 24) 2016*; 1–15.
- 12  
13 691 59. Westin PS, Morris BL, Cox PA, et al. *Development of Computer Program for Floor Plate Response*  
14 692 *from Land Mine Explosions. Technical Report No. 13045*. Warren, MI.
- 15  
16 693 60. Williams K, McClennan S, Durocher R, et al. Validation of a Loading Model for Simulating Blast  
17 694 Mine Effects on Armoured Vehicles. *Int LS-DYNA Users Conf 2009*; 7: 35–44.
- 18  
19 695 61. DoD. *Structures to Resist the Effects of the Accidental Explosions*. 2008. Epub ahead of print 2008.  
20 696 DOI: 10.31142/ijtsrd23455.
- 21  
22 697 62. Teich M, Gebbeken N. Structures subjected to low-level blast loads: Analysis of aerodynamic  
23 698 damping and fluid-structure interaction. *J Struct Eng 2012*; 138: 625–635.
- 24  
25 699 63. Librescu L, Oh S-Y, Hohe J. Linear and non-linear dynamic response of sandwich panels to blast  
26 700 loading. *Compos Part B Eng 2004*; 35: 673–683.
- 27  
28 701 64. Hause T, Librescu L. Dynamic response of anisotropic sandwich flat panels to explosive pressure  
29 702 pulses. *Int J Impact Eng 2005*; 31: 607–628.
- 30  
31 703 65. Hause T, Librescu L. Dynamic response of doubly-curved anisotropic sandwich panels impacted  
32 704 by blast loadings. *Int J Solids Struct 2007*; 44: 6678–6700.
- 33  
34 705 66. Jones N. Strain rate behaviour of materials. In: *Structural Impact*. 1997.
- 35  
36 706 67. Cowper GR, Symonds PS. *Strain rate hardening and strain rate effects in the impact loading of*  
37 707 *cantilever beams*. 1957.
- 38  
39 708 68. Wang ZL, Li YC, Wang JG. Numerical analysis of attenuation effect of EPS geofoam on stress-  
40 709 waves in civil defense engineering. *Geotext Geomembranes 2006*; 24: 265–273.
- 41  
42 710 69. Chen W, Hao H, Hughes D, et al. Static and dynamic mechanical properties of expanded  
43 711 polystyrene. *Mater Des 2015*; 69: 170–180.
- 44  
45 712 70. Overview of materials for Low Carbon Steel. *Material Property Data - MatWeb*,  
46 713 [http://www.matweb.com/search/DataSheet.aspx?MatGUID=034970339dd14349a8297d2c8313](http://www.matweb.com/search/DataSheet.aspx?MatGUID=034970339dd14349a8297d2c83134649)  
47 714 4649.
- 48  
49 715 71. Wickes DIY | Home Improvement Products for Trade and DIY, <https://www.wickes.co.uk/>  
50 716 (accessed 24 October 2019).
- 51  
52 717 72. Craftfoam Blue for Model Making, Product Design & Prototypes,  
53 718 <https://www.panelsystems.co.uk/product/craftfoam-blue> (accessed 7 January 2018).
- 54  
55 719 73. Division AMA. *Phantom Camera Control Help File*. 2011.
- 56  
57 720 74. Ramasamy A, Hill A, Hepper A, et al. Blast Mines: Physics, Injury Mechanisms And Vehicle

- 1  
2  
3 721 Protection. *J R Army Med Corps* 2009; 155: 258–264.  
4  
5 722 75. Bergeron DM, Tremblay JE. Canadian Research to Characterise Mine Blast Output. In:  
6 723 *Proceedings of the 16th International Symposium on the Military Aspects of Blast and Shock.*  
7 724 2000, pp. 501–511.  
8  
9 725 76. Deshpande VS, Mcmeeking RM, Wadley HNG, et al. Constitutive model for predicting dynamic  
10 726 interactions between soil ejecta and structural panels. *J Mech Phys Solids* 2009; 57: 1139–1164.  
11  
12 727 77. Børvik T, Olovsson L, Hanssen AG, et al. A discrete particle approach to simulate the combined  
13 728 effect of blast and sand impact loading of steel plates. *J Mech Phys Solids* 2011; 59: 940–958.  
14  
15 729 78. Rigby S, Fay SD, Tyas A, et al. Localised variations in reflected pressure from explosives buried in  
16 730 uniform and well-graded soils. In: *24th Military Aspects of Blast and Shock.* 2016.  
17  
18 731 79. Hlady SL, Bergeron D, Gonzalez R. *Protecting Vehicles from Landmine Blasts.* 1941.  
19  
20 732 80. Task Group TG-024. *Test Methodologies for Personal Protective Equipment Against Anti-*  
21 733 *Personnel Mine Blast. NATO Report. Final Report of the RTO Human Factors and Medicine Panel*  
22 734 *(HFM),*  
23 735 [http://scholar.google.com/scholar?hl=en&btnG=Search&q=intitle:Test+Methodologies+for+Pers](http://scholar.google.com/scholar?hl=en&btnG=Search&q=intitle:Test+Methodologies+for+Personal+Protective+Equipment+Against+Anti-Personnel+Mine+Blast#0)  
24 736 [onal+Protective+Equipment+Against+Anti-Personnel+Mine+Blast#0](http://scholar.google.com/scholar?hl=en&btnG=Search&q=intitle:Test+Methodologies+for+Personal+Protective+Equipment+Against+Anti-Personnel+Mine+Blast#0) (2004).  
25  
26 737 81. Bergeron D, Walker R, Coffey C. *Detonation Of 100-Gram Anti-Personnel Mine Surrogate Charges*  
27 738 *In Sand: A Test Case For Computer Code Validation. SUFFIELD REPORT No. 668. DRES -SR-668.*  
28 739 1998.  
29  
30 740 82. Absil LHJ, Verbeek HJ, Weerheijm J. Combined Experimental and Numerical Study of Mine  
31 741 Detonations in the Vicinity of Vehicles. In: *15th International Symposium on Military Aspects of*  
32 742 *Blast and Shock.* 1997.  
33  
34 743 83. Gupta AD. Estimation of Vehicle Floor Plate Loading and Response Due to Detonation of a Mine  
35 744 Shallow-Buried in Dry Sand and Wet Tuff. In: *US Army Ground Vehicle Survivability Symposium.*  
36 745 1999.  
37  
38 746 84. Braid MP. *Experimental Investigation and Analysis of the Effects of Anti-Personnel Landmine Blast*  
39 747 *Effects, Suffield Report SSP 2001-188.* 2001.  
40  
41 748 85. Hlady S. Effect of Soil Parameters on Land Mine Blast. *18th Mil Asp Blast Shock.*  
42  
43 749 86. Deshpande VS, Fleck NA. One-dimensional response of sandwich plates to underwater shock  
44 750 loading. *J Mech Phys Solids* 2005; 53: 2347–2383.  
45  
46 751  
47 752  
48  
49  
50  
51  
52  
53  
54  
55  
56  
57  
58  
59  
60



753 **Appendix A. Sand Humidity**

754 **Table A.** Sand humidity around the charge, four points were measured around the charges and one point at the  
 755 centre of the charge, respectively

Test Number	Testing Code	Configuration	Sand humidity (%)
1	SS1	Single steel plate	14.6, 18.3, 16.7, 14.1, 18.7*
2	SS2	Single steel plate	12.3, 13.9, 12.3, 15.1, 12.8*
3	SS3	Single steel plate	13.8, 14.8, 14.6, 12.8, 12.3*
4	SS4	Single steel plate	16.1, 14.6, 18.7, 14.6, 16.6*
5	SA1	Steel - Air gap - Steel	13.5, 14.5, 14.6, 16.3, 14.6*
6	SA2	Steel - Air gap - Steel	14.1, 14.6, 15.6, 14.6, 13.4*
7	SA3	Steel - Air gap - Steel	14.1, 14.4, 13.8, 14.6, 15.7*
8	SF1	Steel - Styrofoam - Steel	14.6, 17.0, 19.5, 16.0, 14.6*
9	SF2	Steel - Styrofoam - Steel	20.3, 19.9, 20.7, 21.0, 14.6*
10	SF3	Steel - Styrofoam - Steel	16.2, 15.2, 16.9, 19.0, 16.7*
11	SX1	Steel - Auxetic core - Steel	19.1, 22.2, 20.8, 18.7, 21.8*
12	SX2	Steel - Auxetic core - Steel	20.5, 19.6, 22.3, 22.5, 23.6*
13	SX3	Steel - Auxetic core - Steel	14.1, 14.6, 16.0, 15.0, 16.8*
14	SX3	Steel - Auxetic core - Steel	12.8, 14.6, 19.1, 26.9, 46.8*

756

757